Rac3 regulates breast cancer invasion and metastasis by controlling adhesion and matrix degradation

Sara K. Donnelly,[1,2] Ramon Cabrera,[1*] Serena P.H. Mao,[1*] John R. Christin,[3] Bin Wu,[4] Wenjun Guo,[3] Jose Javier Bravo-Cordero,[5] John S. Condeelis,[1,2] Jeffrey E. Segall,[1,2] and Louis Hodgson[1,2]

[1]Department of Anatomy and Structural Biology, [2]Gruss-Lipper Biophotonics Center, and [3]Department of Cell Biology, Albert Einstein College of Medicine, Bronx, NY
[4]Biophysics and Biophysical Chemistry, School of Medicine, Johns Hopkins University, Baltimore, MD
[5]Department of Medicine, Division of Hematology and Medical Oncology, Icahn School of Medicine, Tisch Cancer Institute at Mount Sinai, New York, NY

The initial step of metastasis is the local invasion of tumor cells into the surrounding tissue. Invadopodia are actin-based protrusions that mediate the matrix degradation necessary for invasion and metastasis of tumor cells. We demonstrate that Rac3 GTPase is critical for integrating the adhesion of invadopodia to the extracellular matrix (ECM) with their ability to degrade the ECM in breast tumor cells. We identify two pathways at invadopodia important for integrin activation and delivery of matrix metalloproteinases: through the upstream recruiter CIB1 as well as the downstream effector GIT1. Rac3 activity, at and surrounding invadopodia, is controlled by Vav2 and βPIX. These guanine nucleotide exchange factors regulate the spatiotemporal dynamics of Rac3 activity, impacting GIT1 localization. Moreover, the GTPase-activating function of GIT1 toward the vesicular trafficking regulator Arf6 GTPase is required for matrix degradation. Importantly, Rac3 regulates the ability of tumor cells to metastasize in vivo. The Rac3-dependent mechanisms we show in this study are critical for balancing proteolytic activity and adhesive activity to achieve a maximally invasive phenotype.

Introduction

Metastasis is a multistep process where cells escape the primary tumor and disseminate through the body to establish secondary tumors at distant sites. To achieve this, cancer cells form actin-rich protrusions called invadopodia that, in their mature form, degrade the ECM and facilitate local invasion of the cells into the surrounding tissue (Schmitz et al., 2000; Fidler, 2003; Condeelis et al., 2005; Yamaguchi et al., 2005). Although much progress has been made in understanding the molecular mechanisms that regulate invadopodia dynamics in recent years (Chen and Wang, 1999; Ayala et al., 2006; Buccione et al., 2009; Destaing et al., 2011; Linder et al., 2011; Courtneidge, 2012; Hoshino et al., 2013; Beaty and Condeelis, 2014; Bergman et al., 2014; Paz et al., 2014; Hastie and Sherwood, 2016), the mechanisms of how invadopodia transition from initial precursors to mature degradative structures are not fully understood.

Rac3, a member of the p21 Rho family of small GTPases, is an understudied paralog of the canonical Rac1 GTPase and has been implicated in cancer cell invasion (Baugher et al., 2005; Gest et al., 2013; Rosenberg et al., 2017). Rho-family GTPases are molecular switches that cycle between the GTP-bound on state and the GDP-bound off state, regulated by guanine nucleotide exchange factors (GEFs) that activate and GTPase-activating proteins (GAPs) that inactivate them as well as the inhibitory guanine nucleotide dissociation inhibitor (GDI; Hall, 2005). In nonpathological circumstances, Rac3 is primarily expressed in the brain and neuronal tissues (Corbetta et al., 2009; Vaghi et al., 2012). However, up-regulation of Rac3 has been reported in aggressive breast carcinoma as well as prostate and brain cancers (Hwang et al., 2005; Engers et al., 2007; Gest et al., 2013). Despite 93% primary sequence identity between Rac3 and the canonical Rac1, there is evidence to suggest that these paralogs play antagonistic roles. In neuronal differentiation, Rac1 and Rac3 play opposing roles in which Rac3 functions as a negative regulator (Hajdo-Milasinovic et al., 2007). A specific role for Rac3 in autophagy has also been found (Zhu et al., 2011).

In breast cancer, expression of Rac3 is linked to increased tumor invasion in vitro, although its mechanism of action is unknown (Baugher et al., 2005; Chan et al., 2005; Rosenberg et al., 2017). Furthermore, little work has been done to elucidate differential signaling networks involving Rac1 and Rac3. This is intriguing because the Switch I/II regions that mediate regulator and effector binding are identical and thus, they could interact with the same GEFs, GAPs, and downstream effectors.

*R. Cabrera and S.P.H. Mao contributed equally to this paper.

Correspondence to Louis Hodgson: louis.hodgson@einstein.yu.edu

Abbreviations used: DN, dominant negative; FRET, Förster resonance energy transfer; GAP, GTPase-activating protein; GDI, guanine nucleotide dissociation inhibitor; GEF, guanine nucleotide exchange factor; GSH, glutathione; MMP, matrix metalloproteinase; PBD, p21 binding domain; sgRNA, single-guide RNA; TIRF, total internal reflection fluorescence.

The Rockefeller University Press
J. Cell Biol. Vol. 216 No. 12 4331–4349
https://doi.org/10.1083/jcb.201704048

This suggests that differential regulation of these paralogs involves coordinated spatial and temporal control of upstream regulators, downstream effectors, and the GTPases themselves.

In this study, we show that at invadopodia in metastatic breast cancer cells, Rac3 is required to integrate adhesion signaling and ECM degradation. Rac3 is recruited by its specific binding partner, CIB1, and promotes integrin activation at invadopodia. We developed a sensitive monomeric Förster resonance energy transfer (FRET)-based fluorescent biosensor for Rac3 that allowed us to specifically probe the spatiotemporal dynamics of Rac3 activity at invadopodia. We found that activation of Rac3 is coordinated by two GEFs, Vav2 and βPIX, and subsequently active Rac3 modulates vesicular trafficking of MT1–matrix metalloproteinase (MMP) through its effector GIT1. Moreover, we show that Rac3 significantly impacts breast tumor metastasis in vivo. We propose that Rac3 regulates the balance of adhesion and matrix degradation to promote tumor invasion and metastasis.

Results

Rac3 is enriched at invadopodia and required for matrix degradation

Rac3 is known to enhance breast cancer cell invasion (Chan et al., 2005; Gest et al., 2013; Rosenberg et al., 2017); however, the molecular mechanism by which Rac3 promotes invasion is unknown. We hypothesized that Rac3 impacts invasion by regulating the functions of cancer-specific invadopodia, which control ECM degradation. Unlike the canonical Rac1 (Moshfegh et al., 2014), we find that endogenous Rac3 is enriched at the invadopodia core in two different breast cancer cell lines: the rat adenocarcinoma MTLn3 and the human triple-negative MDA–MB-231 (Fig. 1 A; primary antibodies for Rac3 showed negligible cross-reactivity to Rac1—see Fig. S1). To characterize this further, we serum starved MTLn3 cells and stimulated with EGF to induce the synchronous formation of invadopod precursors, which cannot yet degrade the ECM. The number of Rac3-positive invadopodia increased after EGF stimulation (Fig. 1 B), suggesting that Rac3 progressively accumulates at the core in the early stages of invadopodia formation. Next, we used siRNA to deplete Rac3 in both MTLn3 and MDA–MB-231 cells. In both cases, Rac3 depletion resulted in reduced ECM degradation, whereas invadopodia formation (denoted by cortactin and Tks5 colocalization; Oser et al., 2009; Beaty et al., 2013) was unaffected (Figs. 1 C and S2 A), confirming a recent observation (Rosenberg et al., 2017). Depletion of Rac3 had no effect on the expression levels of Rac1, Cdc42, and RhoA (Fig. S2, B and C). Furthermore, we used four individual siRNA oligonucleotides (Fig. S2 D) as well as rescued the defect in matrix degradation by expressing WT but not dominant-negative (DN) Rac3 (Fig. 1 D). Interestingly, the phenotype observed in this study for Rac3 was the opposite of Rac1 depletion, which results in increased ECM degradation without affecting the steady-state number of invadopodia (Fig. 1 D), consistent with previous findings (Moshfegh et al., 2014). Depletion of either Rac1 or Rac3 did not appear to impact the localization of the other protein (Fig. S2 E). Though homologous in primary sequence to Rac1, these data suggest that Rac3 regulates different functions at invadopodia from Rac1 and that Rac3 is dispensable for the formation of invadopodia precursors but is required for the maturation of these structures as defined by their ability to degrade the ECM (Artym et al., 2006; Oser et al., 2009; Mader et al., 2011).

To see whether invadopodia dynamics are impacted in Rac3-depleted cells, we transfected control or Rac3-depleted cells with cortactin-mtagRFP and Tks5-EGFP and imaged the cells every 2 min for 4 h to characterize invadopodia lifetimes. Although depletion of Rac1 was previously shown to stabilize invadopodia and increase their lifetimes (Moshfegh et al., 2014), depletion of Rac3 resulted in invadopodia that were significantly more unstable than those in control cells (Videos 1 and 2). The mean lifetime of steady-state invadopodia in control cells was 50.74 min (± 2.66 min), whereas that in Rac3-depleted cells was 20.64 min (± 7.96 min), a 60% reduction (Fig. 1 E). Further analysis showed that in control cells, 28.3% (± 4.6%) of invadopodia persisted for >1 h, whereas in Rac3-depleted cells, most of the invadopodia lasted for <20 min (Fig. 1 E and Videos 1 and 2). In this experiment, we did not know whether an invadopod recruited Rac3 nor whether that corresponded with long or short lifetimes. To address this, we overexpressed mCherry-Rac3 and saw that invadopodia that recruited Rac3 had a twofold increase in lifetime compared with those that did not (Fig. 1 F). These results indicate that Rac3 promotes structural stabilization of invadopodia, which is important for their transition to mature, degrading states (Bravo-Cordero et al., 2011; Beaty et al., 2013).

Rac3 regulates integrin signaling at invadopodia through CIB1

β1 integrin is known to stabilize invadopodia and promote their maturation by triggering phosphorylation of cortactin via Arg kinase (Beaty et al., 2013). As our data suggest that Rac3 is also important for stabilizing invadopodia, we hypothesized that Rac3 regulates integrin signaling at invadopodia. To test this idea, we stained EGF-stimulated cells for active and total β1 integrin with the invadopodia markers (Fig. 2 A). In control cells, we found that, in agreement with previous work (Beaty et al., 2013), levels of active β1 integrin were increased at invadopodia 5 min after EGF stimulation. In contrast, integrin activation was significantly impaired at invadopodia in Rac3-depleted cells at the same time point (Fig. 2 A). Next, we exogenously activated integrins using Mn^{2+} stimulation (Vallar et al., 1999) and found that this rescued the decrease in invadopodia lifetime observed in Rac3-depleted cells (Fig. 2 B). This indicates that Rac3 is required to promote integrin activation and invadopodia stability.

Although Rac3 has been implicated in the adhesion of neuronal cells (Hajdo-Milasinovic et al., 2007, 2009), a direct role in modulating integrin activation has not been shown. We hypothesized that Rac3 may regulate integrin activity though its specific binding partner calcium and integrin binding protein 1 (CIB1). This protein interacts with Rac3 but not with Rac1 (Haataja et al., 2002). CIB1 also has the ability to interact with many α integrin chains and regulates integrin activity (Freeman et al., 2013). We first investigated whether CIB1 plays a role at invadopodia. We found that CIB1 localizes to invadopodia (Fig. 2 C); however, in contrast with Rac3, CIB1 is recruited to invadopodia precursors independent of EGF stimulation (Fig. 2 D). CIB1 is enriched at ∼30% of invadopodia in both starved and EGF-stimulated cells (Fig. 2 D), similar to the steady-state proportion of invadopodia containing Rac3 (not depicted). This suggests that CIB1 is recruited to invadopodia upstream of Rac3. When CIB1 was depleted, cells phenocopied the defect in ECM degradation observed in Rac3-depleted

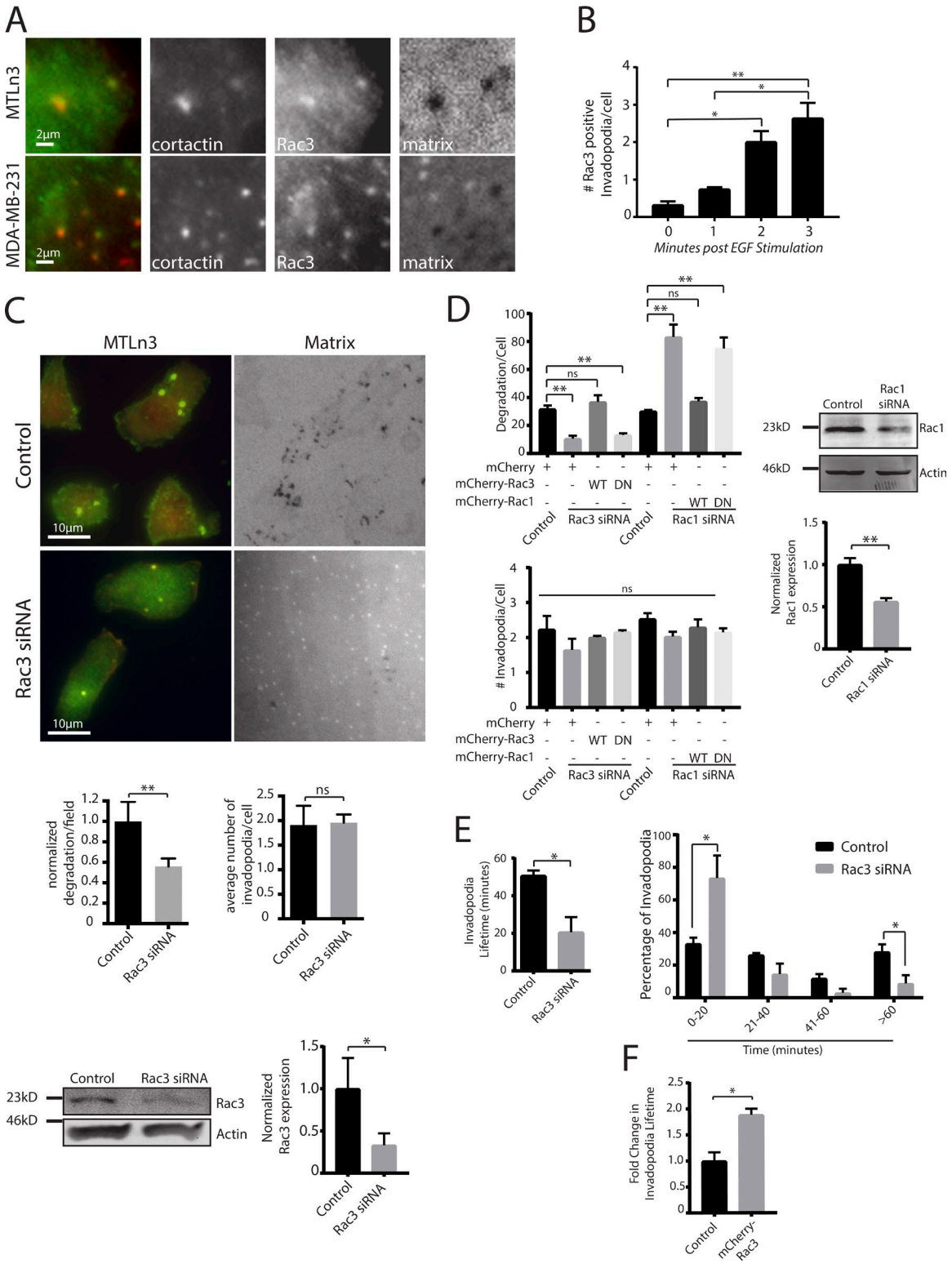

Figure 1. **Rac3 is enriched at invadopodia and required for matrix degradation.** (A) Endogenous Rac3 accumulated at invadopodia in MTLn3 or MDA–MB-231 cells plated on a 405-nm fluorescent gelatin matrix. Invadopodia are denoted by cortactin colocalization with spots of matrix degradation. (B) Quantification of endogenous Rac3 accumulation at invadopodia in MTLn3 cells stimulated with 5 nM EGF for the indicated times. $n \geq 30$ invadopodia from ≥20 cells for each condition; three independent experiments. (C, images) MTLn3 cells transfected with control (top) or Rac3 siRNA (bottom) and plated on 405 nm fluorescent gelatin overnight. (C, bottom left) Normalized, mean degradation area/field. $n \geq 10$ fields for each condition; three independent experiments. (C, bottom right) Mean number of invadopodia/cell. $n \geq 50$ invadopodia from ≥25 cells for each condition; three independent experiments. Western blot of cell lysates of control and Rac3 siRNA–treated MTLn3 cells blotted for Rac3 and β-actin with quantification. (D) Rescue of siRNA Rac3 or Rac1 depletion by expression of WT or DN Rac3 or Rac1, respectively. (D, top) Degradation area/cell. $n \geq 20$ cells for each condition; three independent experiments. (D, bottom) Mean number of invadopodia/cell. $n \geq 25$ invadopodia from ≥20 cells for each condition; three independent experiments. (D, right) Western blot of cell lysates of control and Rac1 siRNA–treated MTLn3 cells blotted for Rac1 and β-actin, with quantification below. (E, left) Mean

cells. Although the numbers of invadopodia formed are similar in control and CIB1-depleted cells, ECM degradation was reduced by 81% (± 2.2%; Fig. 2 E). Furthermore, as with Rac3, depletion of CIB1 resulted in decreased invadopodia lifetimes (Fig. 2 F and Video 3).

We wanted to determine whether CIB1 is an upstream regulator or downstream effector of Rac3 at invadopodia. A previous study concluded that CIB1 is a downstream effector of Rac3 after showing that it can interact with constitutively active Rac3 (Haataja et al., 2002). However, Haataja et al. (2002) did not demonstrate whether a DN mutant of Rac3 (T17N) could bind CIB1. Pulldown experiments in cells overexpressing Rac3 and CIB1 showed that CIB1 interacts with WT Rac3 as well as both the DN (T17N) and the constitutively active mutants (Q61L or G12V) of Rac3 (Fig. S2 F). These results show that Rac3 and CIB1 binding is independent of Rac3 activation. Because CIB1 does not interact with Rac1, which differs from Rac3 primarily at the C-terminal polybasic hypervariable region (Haataja et al., 1997, 2002), the Rac3–CIB1 interaction may depend on their cellular localizations, which are likely determined also by the N-terminal myristoylation of CIB1 and the interaction of Rac3 with cytoplasmic GDI (Zhang et al., 2009) as well as insertion into appropriate membrane domains. Based on our result and the observation that CIB1 is recruited to invadopodia before Rac3 during EGF-dependent invadopodia precursor formation (Fig. 2 D), we hypothesized that CIB1 may help recruit Rac3 to invadopodia. Indeed, in CIB1-depleted cells, the number of Rac3-positive invadopodia was significantly reduced (Fig. 2 G). Although additional mechanisms may also mediate Rac3 recruitment to invadopodia, these data show that CIB1 localizes Rac3 to invadopodia, where it promotes integrin activation and stabilization of these structures.

Rac3 biosensor reveals two spatially distinct pools of activity at invadopodia

To better understand the role of Rac3, we wished to determine its activation dynamics at invadopodia. We developed a monomeric single-chain genetically encoded FRET-based biosensor that is specific for Rac3. This biosensor was similar to the design of our Rac1 (Moshfegh et al., 2014) and Rac2 (Miskolci et al., 2016) sensors and consisted of a monomeric Cerulean1 and monomeric circularly permuted (cp229) Venus fluorescent protein FRET pair with the p21 binding domain (PBD) of p21-activated kinase-1 (PAK1) and a full-length Rac3 (Fig. 3 A). In this biosensor, (A) fluorescent proteins retained the monomeric mutation (A206K) to prevent spuriously high FRET through aggregation when inserted into membrane domains, (B) reversibility between the on and off states was achieved by monomeric components and fine-tuning of the binding domain affinity by incorporation of an autoinhibitory structure, and (C) an intact C terminus of Rac3 allowed for interaction with GDI and for insertion into appropriate membrane domains. Extensive fluorometric characterization of the Rac3 biosensor revealed an almost twofold difference between the on (Q61L) and the off states (T17N or plus excess GDI) of the biosensor (Fig. 3 B). Two different constitutively active mutants (G12V or Q61L) showed increased FRET when compared with the WT Rac3 biosensor, but GDI coexpression impacted FRET only for the WT and G12V (binds GDI) but not Q61L (does not bind GDI; Fig. S3 A). The T17N DN and two effector-binding mutants (T35S and Y40C) showed reduced FRET (Fig. S3 A). Coexpression of Rac-targeting but not Rho- or Cdc42-targeting GEFs resulted in increased FRET in the presence or absence of GDI (Fig. S3, B and C). Coexpression of p50RhoGAP (targets Rac) also reduced FRET, whereas expression of p190RhoGAP or Rap1GAP (not Rac targeting) had no effect (Fig. S3 D). To confirm that expression of the Rac3 biosensor did not result in aberrant downstream signaling, we performed a pulldown assay using purified exogenous PBD. The Rac3 biosensor only interacted with an exogenous effector when both PBDs within the biosensor were mutated (2× PBD, H83D/H86D) so they could not bind active Rac3 (Fig. S3 E). When expressed in breast cancer cell lines (MTLn3/MDA–MB-231), we observed an ∼30% difference between the constitutively active versus DN versions of the Rac3 biosensor (Fig. S3, F and G). The biosensor also responded to stimulation with serum after starvation (Fig. S3 H). Finally, we applied the synonymous codon modification (Wu et al., 2015) to prevent homologous recombination during transfection and transduction. Thus, we have generated a functional, reversible, and specific biosensor that can be used to explore the activity dynamics of Rac3 with high spatiotemporal resolution.

We first studied the activity patterns of Rac3 at steady-state invadopodia using total internal reflection fluorescence (TIRF) microscopy of fixed samples. As previously described (Bravo-Cordero et al., 2011), we defined two regions of invadopodia measurements. The "core" of the invadopod corresponds with the region defined by the cortactin/Tks5 staining and is the central part the structure. The "ring"-like region was defined as a radius of 1.74 µm (8 pixels) around the invadopodia core. By taking a ratio of the mean FRET/donor intensity in the core to the ringlike region, we identified two pools of Rac3 activity at these structures (Fig. 3 C), in contrast with a previous observation where only ring-localized Rac3 activity was reported (Rosenberg et al., 2017). We calculated the SD of the activity distribution within the populations and used 1.0 ± 1 SD as the cutoff for high core or ring activity. At 4.8% (± 3.8%) of invadopodia, high Rac3 activity was observed in the core of the structure, whereas in 17.8% (± 6.9%) of invadopodia, a ring of Rac3 activity surrounding the core was observed (Fig. 3, C and D). No difference in the ratio of core/ring Rac3 activity was observed at the other 77.4% (± 8.7%) of invadopodia. This suggests dynamic regulation of Rac3 activity at invadopodia. Interestingly, the ring pattern of Rac3 activity was more distinct in cells expressing a constitutively active biosensor (Fig. S3 I), indicating that forced activation of Rac3 results in stable, localized activity in the ring compartment. Consistent with the fixed data, live imaging showed Rac3 activity in both the core and the ring region of invadopodia. As Rac3 activities in the ring region appeared stochastic, we first took the time-lapse series of activity data and maximally projected it in time. The ringlike localization of Rac3 activity was more readily visualized and quantified in this manner (Fig. 3 E), similar to the previously observed ring localization of RhoC activity (Bravo-Cordero et al., 2011). Maximum projections of regions

invadopodia lifetime. $n \geq 30$ invadopodia from ≥10 cells for each condition; three independent experiments. (E, right) Same data shown as histogram with bins corresponding with invadopodia lifetimes in 20-min intervals. (F) Fold change in lifetime of invadopodia containing mCherry-Rac3 in MTLn3 cells. $n = 29$ invadopodia from ≥10 cells for each condition; three independent experiments. *, $P \leq 0.05$; **, $P \leq 0.01$. All error bars are SEM.

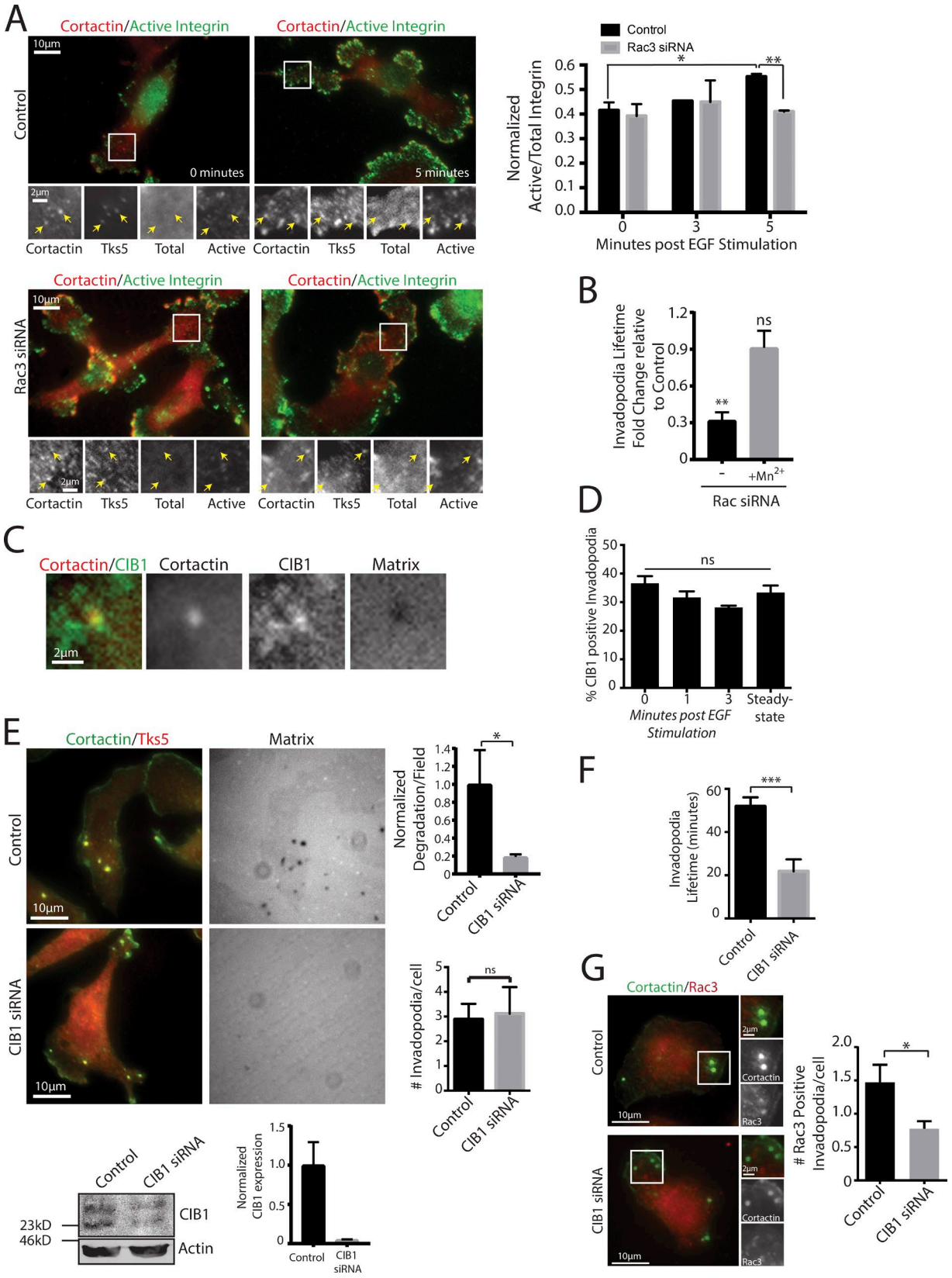

Figure 2. **Rac3 regulates integrin signaling at invadopodia through CIB1.** (A, images) Images of control (top) or Rac3 siRNA (bottom)–treated MDA–MB-231 cells plated on gelatin, starved, and stimulated with EGF for 0 min (left) or 5 min (right). Cells were stained for active or total integrin as well as cortactin and Tks5 to denote invadopodia. Yellow arrows indicate invadopodia. (A, graph) The ratio of active/total integrin at invadopodia in control or Rac3 siRNA–treated cells. $n \geq 25$ invadopodia from ≥5 cells for each condition; three independent experiments. (B) Exogenous Mn^{2+} treatment rescues invadopodia lifetimes in Rac3-depleted cells. $n \geq 98$ invadopodia from ≥3 cells for each condition; three independent experiments. (C) Images of endogenous CIB1 at invadopodia (cortactin/matrix) in MTLn3 cells. (D) Endogenous CIB1 accumulation at invadopodia in MTLn3 cells stimulated with 5 nM EGF

without invadopodia showed random FRET patterns, indicating the ringlike activity of Rac3 is specific to these structures (Fig. S3 J). We then used autocorrelation analysis of the fluctuation in Rac3 activity within the ring region as a function of time, and this analysis quantitatively indicated a stochastic and nonoscillatory behavior in the ring (Fig. 3 F, left). Using the same autocorrelation analysis, the core-associated Rac3 activity showed a distinct, oscillatory periodicity of 12 ± 3 min (Fig. 3 F, right). The differential Rac3 activity dynamics in the core versus the ring region of invadopodia suggests distinct Rac3 regulatory mechanisms in these compartments.

Vav2 and βPIX GEFs concertedly regulate Rac3

To identify the regulators of Rac3 activity at invadopodia, we turned to two candidate GEFs, Vav2 and βPIX, that have been shown to be important in integrin-dependent signaling pathways (Abe et al., 2000; Mayhew et al., 2006; Rosenberger and Kutsche, 2006; Jones et al., 2013). Vav2 traditionally targets the canonical Rho-GTPases RhoA, Rac1, and Cdc42, associates with β1 integrin, and is a downstream target of EGFR signaling, both of which are important in invadopodia regulation. Recently, Vav2 was implicated in Rac3 activation at invadopodia in a ringlike region around the core, although Vav2 does not localize to this ringlike structure (Rosenberg et al., 2017). We also confirmed that the endogenous and EGFP-Vav2 are localized at the core of invadopodia and not in a ring (Fig. 4 A) and that its depletion results in decreased ECM degradation (Fig. 4 C), similar to previous findings (Rosenberg et al., 2017). βPIX is a GEF for Rac1 and Cdc42 (Shin et al., 2002) and associates with GIT1 and paxillin at focal adhesions (Botrugno et al., 2006; Mayhew et al., 2006). Previously and in this study, we found that depletion of βPIX also decreases ECM degradation (Fig. 4 C; Moshfegh et al., 2014). As with active Rac3, we observed that βPIX localized both in the core and in the ring region around invadopodia in both MDA–MB-231 and MTLn3 cells (Fig. 4 B).

To see whether these GEFs impact Rac3 activity, we depleted them using siRNA and then used our biosensor to determine any changes in Rac3 activity at the core or ring region around invadopodia. As before, we determined the population of invadopodia that showed high Rac3 activity either in the core or the ring for control, Vav2, or βPIX-depleted cells (Fig. 4 D). When Vav2 was depleted, the population with higher Rac3 activity in the ring region was unaffected, but the population of invadopodia with higher Rac3 activity in the core was significantly reduced (Fig. 4 D). This indicates that Vav2 primarily regulates Rac3 activity in the core of invadopodia. Conversely, when βPIX was depleted, the percentage of invadopodia with higher Rac3 activity in the core was unaffected, but the percentage with higher Rac3 activity in the ring region was significantly reduced, indicating that βPIX primarily regulates Rac3 activity within the ring region (Fig. 4 D). The whole-cell intensity of Rac3 activity was unaffected by depletion of either GEF (Fig. 4 D), suggesting a mechanism by which two GEFs spatially regulate Rac3 activation at invadopodia with a high degree of specificity.

Rac3 regulates MT1-MMP–mediated matrix degradation via GIT1

Our data suggest that Rac3 is recruited to invadopodia by CIB1 and that this promotes invadopodia stability by regulating integrin signaling. However, this interaction with CIB1 was not dependent on the activation status of Rac3 (Figs. 2 G and S2 F). Based on our observation of highly localized and dynamic Rac3 activity patterns at invadopodia regulated by two upstream GEFs, we hypothesized that Rac3 activity is also critical to regulating invadopodia function, likely through an activity-dependent interaction with a downstream effector molecule. Because depletion of Rac3 resulted in a defect in ECM degradation (Fig. 1 C), we investigated whether recruitment of MT1-MMP, the enzyme predominantly responsible for matrix degradation (Castro-Castro et al., 2016), is impacted by loss of Rac3. We quantified the levels of endogenous, extracellular MT1-MMP at invadopodia in control or Rac3-depleted cells and found a significant reduction in the amount of MT1-MMP at invadopodia in Rac3-depleted cells (Fig. 5 A). This suggests that Rac3, via its downstream signaling pathway, regulates MT1-MMP delivery and/or presentation at invadopodia to impact matrix degradation.

Recent work has shown that delivery of MT1-MMP to the cell surface is dependent on the small GTPase Arf6 (Marchesin et al., 2015). Arf6 localizes to invadopodia, and depletion of Arf6 results in decreased matrix degradation, similar to Rac3 depletion (Hashimoto et al., 2004). As such, we decided to focus on GIT1, a molecule that interacts with Rac3 in a GTP-dependent manner and contains an Arf-GAP domain specific to Arf6 (Vitale et al., 2000; Hajdo-Milasinovic et al., 2009). We hypothesized that Rac3 regulates trafficking or exocytosis of MT1-MMP at invadopodia via GIT1, which regulates the GTP cycling of Arf6 through its GAP domain. Consistent with a function downstream of Rac3, depletion of either GIT1 or Arf6 resulted in normal formation of invadopodia but decreased ECM degradation (Figs. 5 B and S4 A). Expressing EGFP-GIT1 in the GIT1-depleted background rescued the loss of degradation (Fig. 5 C). Importantly, we found that EGFP-GIT1 localized to invadopodia in two distinct pools: at the core of invadopodia and in a ringlike region around invadopodia (Figs. 5 D and S4 B), similar to Rac3 activity at these structures (Fig. 3 C). Furthermore, EGF stimulation of MTLn3 cells showed that GIT1 translocated from primarily ring localization in starved cells to predominantly core localization after 3 min of EGF stimulation (Fig. 5 E). However, live imaging demonstrated that GIT1 was not retained in the core but that it oscillated at invadopodia, remaining a mean of 16.4 min (±2.27 min) in the ring and 3.7 min (± 0.34 min) in the core of steady-state invadopodia (Fig. 5 F, Fig. S4 C, and Video 4). The dwell time of GIT1 in

for the indicated times or plated overnight on gelatin (steady state). $n \geq 50$ invadopodia from ≥25 cells for each condition; three independent experiments. (E) MTLn3 cells transfected with control (top) or CIB1 siRNA (bottom) and plated on 405 nm fluorescent gelatin overnight. (E, top) Normalized, mean degradation area/field. $n \geq 10$ fields for each condition; three independent experiments. (E, bottom) Mean number of invadopodia/cell. $n \geq 50$ invadopodia from ≥25 cells for each condition; three independent experiments. Western blot of cell lysates of control or CIB1 siRNA–treated MTLn3 cells blotted for CIB1 or β-actin with quantification. (F) Invadopodia lifetime when CIB1 is depleted. $n \geq 30$ invadopodia from ≥10 cells for each condition; three independent experiments. (G) Images of endogenous Rac3 localization at invadopodia in control or CIB1-depleted cells. Quantification of number of invadopodia/cell positive for endogenous Rac3 in MTLn3 cells treated with control or CIB1 siRNA. $n \geq 75$ invadopodia from ≥27 cells for each condition; three independent experiments. *, $P \leq 0.05$; **, $P \leq 0.01$; ***, $P \leq 0.01$. All error bars are SEM.

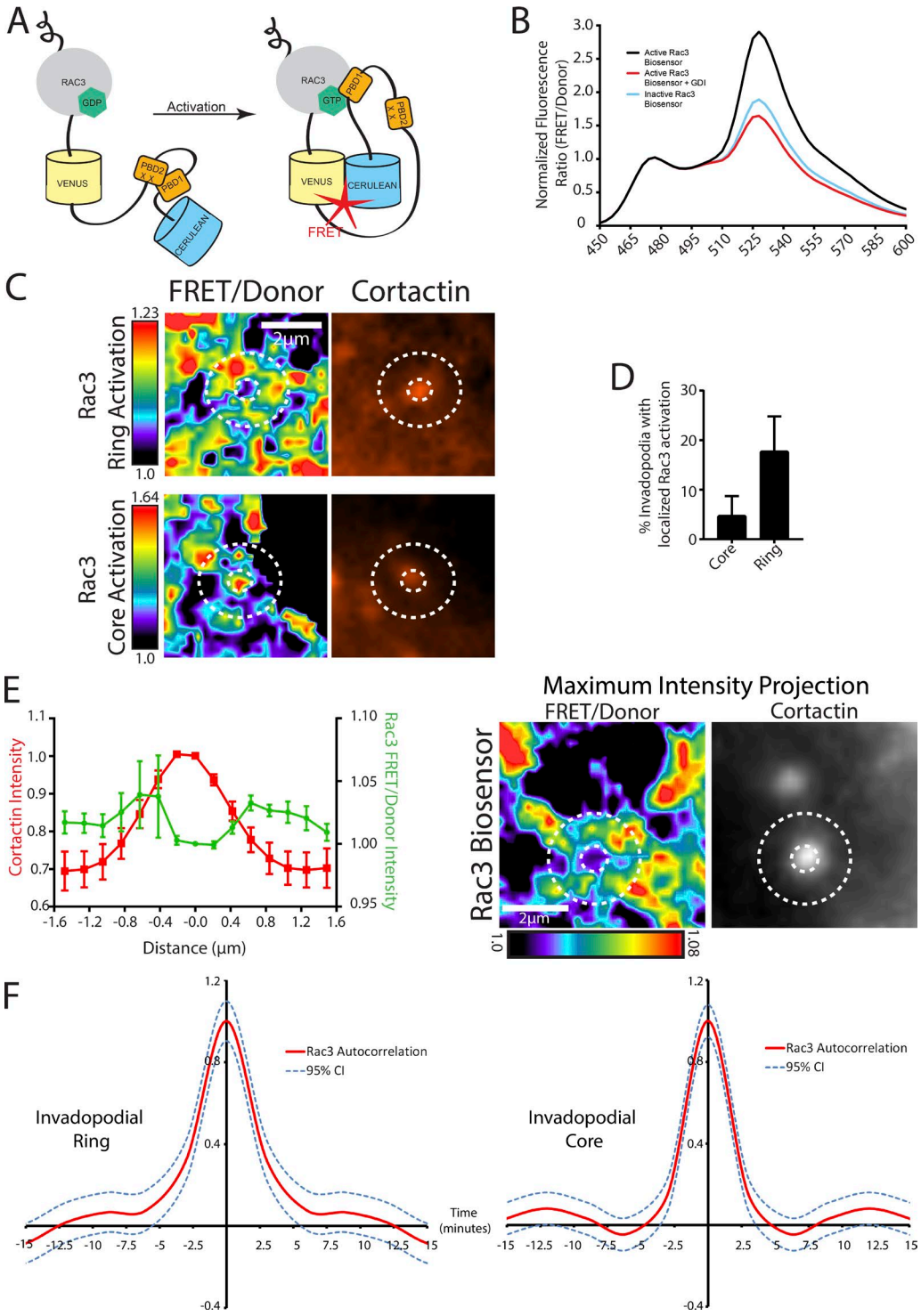

Figure 3. **Rac3 FRET biosensor reveals two spatially distinct pools of Rac3 activity at invadopodia.** (A) Biosensor design: inactive (left) and active (right) conformations. Black Xs indicate H83D/H86D GTPase binding–deficient mutations. Cyan cylinders indicate monomeric Cerulean fluorescent protein, and yellow cylinders indicate circularly permuted (cp229) monomeric Venus fluorescent protein. (B) Representative normalized emission spectra of biosensor mutants in HEK293 cells excited at 433 nm and normalized to donor emission at 474 nm. G12V (active, black line), T17N (inactive, blue line), and G12V coexpressed with 2× excess GDI (red line) are shown. (C) Representative image of an invadopodium showing the two spatially distinct pools of Rac3 activity in MDA–MB-231 cells. (C, top) Ringlike region of Rac3 activity around the invadopod. (C, bottom) Rac3 activity at the invadopod core (denoted by cortactin). Dashed lines indicate core and ringlike invadopod regions. (D) Percentage of invadopodia with high core or ring Rac3 activation. $n \geq 100$ invadopodia from ≥10 cells; three independent experiments. (E, left) Linescan measurement along invadopodia of maximum-intensity projections of Rac3 activity and cortactin fluorescence. $n = 7$ invadopodia from ≥5 different cells imaged on ≥3 independent days. (E, right) Maximum-intensity projection of FRET/donor ratio for Rac3 at an invadopod. Projection is 21 frames (1 min/frame). (F, left) Autocorrelation function of the fluctuation of Rac3 activity in the ringlike region around the invadopodia. The autocorrelation function did not inflect after the zero crossing (no periodicity). $n = 9$ invadopodia ring measurements from ≥6 different cells; three or more independent experiments. (F, right) Autocorrelation function of the fluctuation of Rac3 activity within the invadopodia core. Period of oscillation: 12 min ± 3 min (±SD). $n = 6$ invadopodia core measurements from ≥5 different cells; three or more independent experiments. All error bars are SEM. CI, confidence interval.

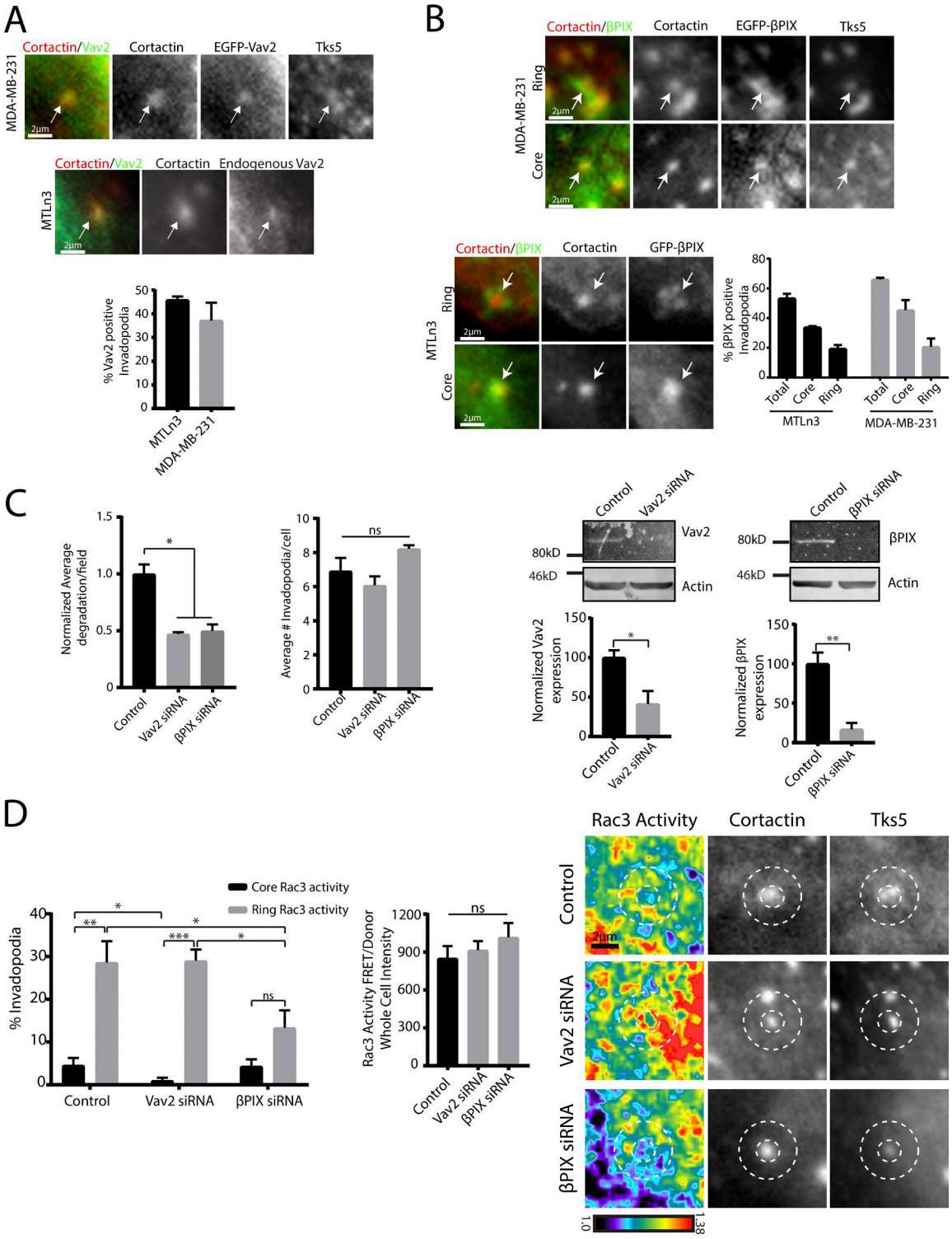

Figure 4. **Vav2 and βPIX GEFs work in concert to regulate Rac3 at invadopodia.** (A) Image of EGFP-Vav2 localized to invadopodia core in MDA–MB-231 cells plated on gelatin for 6 h or MTLn3 cells plated on gelatin for 16 h. The bottom graph shows quantification of the percentage of Vav2-positive invadopodia in the indicated cell line. (B) Image of EGFP-βPIX localized to the ring (top) or core (bottom) of invadopodia in MDA–MB-231 cells plated on gelatin for 6 h or MTLn3 cells plated on gelatin for 16 h. White arrows indicate invadopodia. Quantification of the percentage of βPIX-positive invadopodia in the indicated cell line. (C, left) Normalized mean degradation area per field in MDA–MB-231 cells with control, Vav2, or βPIX siRNA and plated on 405 nm fluorescent gelatin for 6 h. $n \geq 10$ fields for each condition; three independent experiments. (C, right) The mean number of invadopodia per cell for the same conditions. $n \geq 50$ invadopodia from ≥25 cells for each condition; three independent experiments. Western blot of cell lysates of control, Vav2 (top), or βPIX (bottom) siRNA–treated MDA–MB-231 cells blotted for Vav2, βPIX, or β-actin with quantification. (D, right) The percentage of invadopodia with high core (black bars) or high ring (gray) Rac3 activity in MDA–MB-231 cells with control, Vav2, or βPIX siRNA. $n \geq 18$ invadopodia in ≥5 cells; three independent experiments. Data were analyzed using a one-tailed paired Student's *t* test. (D, left) Whole-cell intensity quantification of Rac3 activity in control, Vav2, or βPIX-depleted cells. Representative images of Rac3 activity in control (top), Vav2 siRNA (middle), or βPIX siRNA (bottom)–treated cells. Dashed lines indicate the invadopodium core and ring. All Rac3 activity images are scaled identically. *, $P \leq 0.05$; **, $P \leq 0.01$; ***, $P \leq 0.001$. All error bars are SEM.

the invadopodia core is similar to that of Rac3 activation in this location, suggesting that GIT1 translocation between the core and ring could be mediated by the periodic modulation of upstream Rac3 activity. Consistent with a role for Rac3 activity in regulating GIT1 localization, depletion of Rac3 or expression of a Rac3 mutant that is deficient in effector binding (T35S/Y40C; White et al., 1995) resulted in predominantly core localization of GIT1, although the percentage of GIT1-positive invadopodia was not altered (Figs. 5, G and H). Furthermore, depletion of GIT1 did not affect localization of Rac3 at invadopodia (Fig. S4 D), strengthening the hypothesis that GIT1 functions as an effector of Rac3 at these structures. Moreover, we produced CRISPR/Cas9 genetic deletion of Rac3 in MTLn3 cells (Fig. S5, A–C) and expressed mutants of Rac3, including the T35S/Y40C mutant. This version of Rac3 was not able to rescue the matrix degradation defect (Fig. S5 D), indicating that Rac3–effector interaction is required for the ring localization of GIT1 and for matrix degradation. The nontargeting control and Rac3 knockouts showed appropriate phenotypes, similar to control and Rac3 siRNA (Fig. S5 C), and did not impact expression levels of other Rho GTPases (Fig. S5 B).

To determine whether GIT1 Arf-GAP activity is required for invadopodia function, we overexpressed EGFP-GIT1-R39K (Arf-GAP–deficient mutant; Hajdo-Milasinovic et al., 2009) in MTLn3 cells. Similar to depletion of GIT1, inhibition of its Arf-GAP activity resulted in decreased matrix degradation compared with cells overexpressing WT EGFP-GIT1 (Fig. 5 I). These data agree with previous studies demonstrating that GTP–GDP cycling by Arf6 is important for invadopodia-dependent matrix degradation (Hashimoto et al., 2004; Marchesin et al., 2015). Finally, we investigated whether Rac3, GIT1, and Arf6 regulate surface presentation of MT1-MMP at invadopodia or trafficking of MT1-MMP to these structures. We expressed MT1-MMP–GFP (Bravo-Cordero et al., 2007) in cells treated with Rac3, GIT1, or Arf6 siRNA and stained for surface MT1-MMP before permeabilization. Depletion of either Rac3 or GIT1 resulted in reduced extracellular but not intracellular MT1-MMP at invadopodia (Fig. 5 J). In contrast, both surface and intracellular levels of MT1-MMP at invadopodia were reduced in Arf6-depleted cells (Fig. 5 J). These data suggest that Rac3 and GIT1 specifically regulate surface presentation of MT1-MMP at invadopodia. The Arf6 data are consistent with a previous study showing that this protein regulates trafficking of MT1-MMP to the plasma membrane (Marchesin et al., 2015); however, given the localization of Arf6 to invadopodia (Fig. S4 A), it is likely that Arf6 plays a role in both trafficking and surface presentation of MT1-MMP at invadopodia.

Rac3 promotes invasion and metastasis of breast cancer cells

To evaluate the functional relevance of the signaling axes involving Rac3, we first sought to determine the ability of tumor cells to invade through ECM. We used the in vitro invasion assay where tumor cells migrate in response to serum through a Matrigel-coated filter in culture (Bravo-Cordero et al., 2011). Compared with the control siRNA-treated condition, depletion of Rac3 significantly impacted the ability of MTLn3 cells to invade through the matrix (Fig. 6 A) as expected from their reduced matrix degradation capacity and reduction in MT1-MMP presentation at invadopodia. Importantly, we observed that depletion of other signaling axes members, Vav2, βPIX, CIB1, GIT1, and Arf6 GTPase, also resulted in reduced invasion through Matrigel-coated filters (Fig. 6 A). We next investigated whether overexpressing constitutively activated Rac3 in an otherwise noninvasive, normal epithelial MCF10A cells would result in a gain of function. Unlike MDA–MB-231 and MTLn3 cells, MCF10A cells do not express Rac3 (Fig. 6 B; Gest et al., 2013). When G12V or Q61L mutant of Rac3 was expressed in MCF10A cells, we observed formation of cortactin and Tks5-positive invadopodia and associated matrix degradation (Fig. 6 B). Importantly, overexpression of constitutively active Rac1 (Q61L) did not result in the induction of invadopodia in these cells (Fig. 6 B). These results corroborate the functional impact of the pathways controlled by Rac3 signaling axes, important for invasion of breast tumor cells.

Finally, we sought to determine whether Rac3 is important in the mouse model of breast tumor metastasis. We used the MTLn3 cells knocked out for Rac3 using CRISPR/Cas9 (Fig. S5), stably expressed EGFP, and orthotopically injected into the mammary fat pad of 6–8-wk-old female severe combined immune deficiency mice. We found that lung metastasis was significantly reduced in mice bearing the Rac3-knockout MTLn3 tumors compared with the nontargeting control tumors (Fig. 6 C). Validating our in vitro invasion defects (Fig. 6 A), circulating tumor cells were also significantly reduced in mice bearing the Rac3-knockout MTLn3 cells (Fig. 6 C), suggesting defects in their ability to invade and intravasate during the early stages of metastasis. Collectively, this demonstrates that pathways regulated by Rac3 (Fig. 6 D) have a significant, functional impact on breast tumor dissemination and metastasis.

Discussion

Invadopodia are actin-rich structures critical for tumor cell invasion and dissemination in many cancers including breast, prostate, head and neck, and melanoma (Clark et al., 2007; Desai et al., 2008; Bravo-Cordero et al., 2011; Gligorijevic et al., 2012; Moshfegh et al., 2014; Jimenez et al., 2015; Nicholas et al., 2016). They are specialized, coordinated, and regulated organelles that are required to breach basement lamina (Lohmer et al., 2014), for localized probing and degradation of the ECM microenvironments (Parekh et al., 2011), and cell–cell interactions (Roh-Johnson et al., 2014) during many phases of the metastatic cascade. The protease-dependent phase of the cascade (Gimona et al., 2008; Yu et al., 2012) requires cells to sense their microenvironment in order to spatially and temporally regulate ECM degradation and forward migration. In fact, both integrin and growth factor signals are integrated by invadopod core proteins to define tumor cell invasion (Eddy et al., 2017). Thus, we hypothesized that a molecular mechanism exists that balances cell–ECM adhesion and ECM degradation during tumor invasion. In this study, we define a novel role for Rac3 as a central node that links adhesion-based sensing of the ECM to surface presentation of MT1-MMP, a key enzyme required to degrade the ECM.

Invadopodia are formed in a stepwise manner with the initial establishment of a precursor complex followed by the transition to a mature invadopod that can degrade the ECM (Eddy et al., 2017). This transition is controlled by Arg-dependent phosphorylation of tyrosine-421 of cortactin, resulting in recruitment of the Nck–N-WASP complex followed by integrin-talin–NHE-1–mediated release of activated cofilin from cortactin, driving actin polymerization, stabilization, and

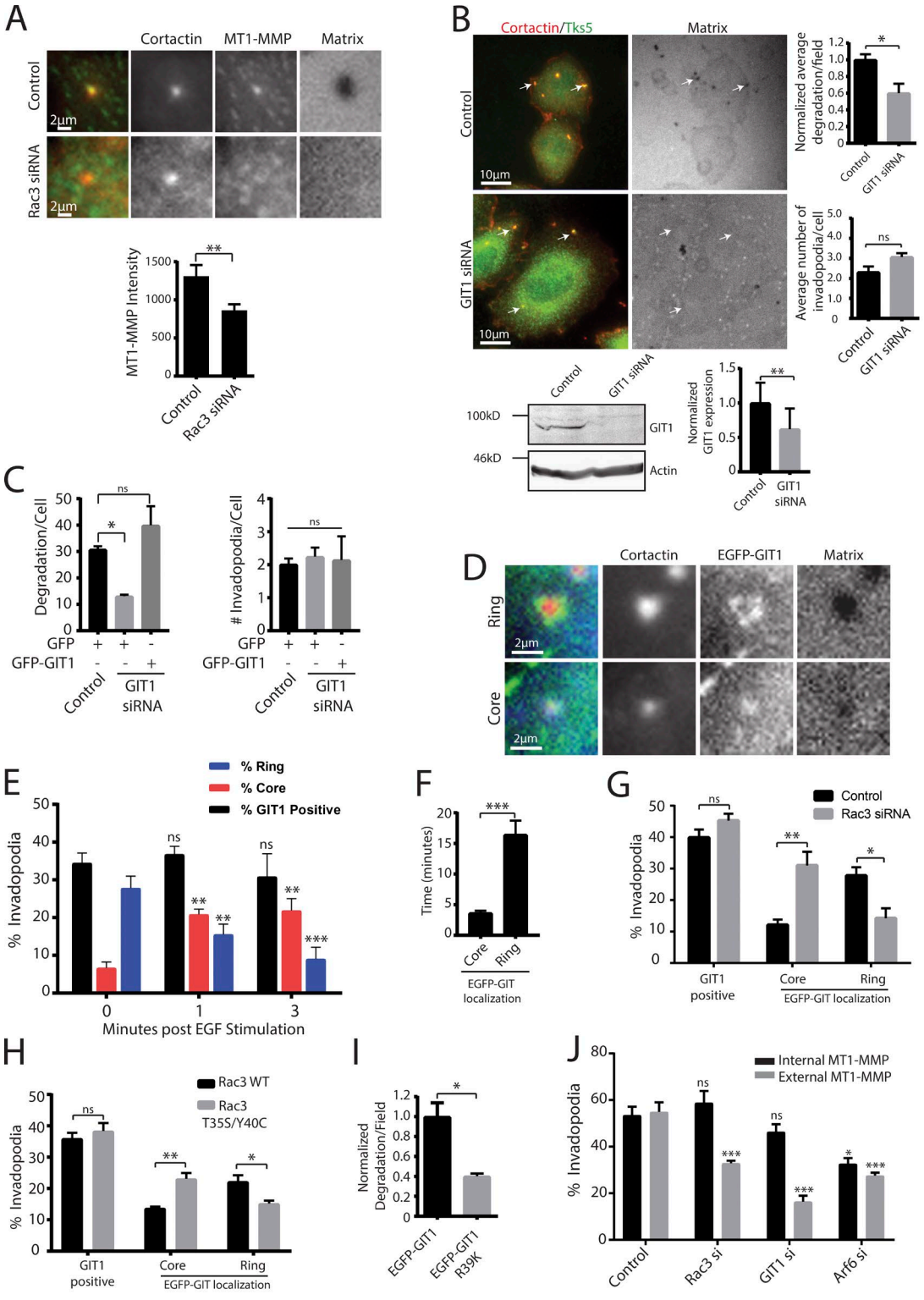

Figure 5. **Rac3 targets GIT1 to regulate MT1-MMP–mediated matrix degradation at invadopodia.** (A) Images of control (top) or Rac3 siRNA (bottom)–treated MTLn3 cells plated on 405 nm fluorescent gelatin for 16 h. Cells were stained with anti–MT1-MMP antibody for 30 min before fixation. Quantification of the intensity of MT1-MMP at invadopodia in control or Rac3 siRNA–treated cells. $n \geq 20$ in ≥8 cells; three independent experiments. (B) MTLn3 cells with control (top) or GIT1 siRNA (bottom) and plated on 405 nm fluorescent gelatin overnight. White arrows indicate invadopodia. (B, left) Normalized mean degradation area per field. $n \geq 10$ fields for each condition; three independent experiments. (B, right) Mean number of invadopodia per cell. $n \geq 50$ invadopodia from ≥25 cells for each condition; three independent experiments. (B, bottom) Western blots of cell lysates of control and GIT1 siRNA–treated MTLn3 cells blotted for GIT1 and β-actin with quantification. (C) Expression of GFP-GIT1 rescues the matrix degradation defect when GIT1 is depleted. $n \geq 36$ invadopodia fields and ≥21 cells for each condition; three independent experiments. (D) Representative MTLn3 cells expressing EGFP-GIT1 and plated on 405 nm fluorescent gelatin for 16 h. (D, top) Ringlike localization of EGFP-GIT1. (D, bottom) Core localization of EGFP-GIT1 at invadopodia.

maturation of invadopodia (Beaty and Condeelis, 2014). We now demonstrate that recruitment of Rac3 to invadopodia is also critical for the stabilization of invadopodia structures through the regulation of inside-out integrin signaling. Depletion of Rac3 results in unstable, short-lived invadopodia that cannot degrade the ECM. We show that this stems from defects in integrin activation at these structures in the absence of Rac3 recruitment to invadopodia. Our data suggest that recruitment of Rac3 via its interaction with CIB1 is important for efficient integrin signaling at invadopodia. As Rac3 accumulates at invadopodia in response to EGF stimulation, this suggests that Rac3 is an important node connecting EGFR signaling with adhesion signaling at invadopodia.

Furthermore, we show that active Rac3 spatially regulates its downstream effector GIT1 to mediate surface presentation of MT1-MMP and ECM degradation at invadopodia. We show that the Arf-GAP activity of GIT1 is required for efficient matrix degradation, supporting a model in which Rac3 and GIT1 control the spatial localization of Arf6 activity, likely important for regulating the delivery of MT1-MMP to invadopodia (Marchesin et al., 2015). Because GIT1 is a downstream effector of Rac3, we asked how the activity of Rac3 at invadopodia is regulated and whether this impacts GIT1 recruitment to invadopodia and its activation of the downstream signaling pathway involving GIT1–Arf-GAP functions. We approached this question by developing a genetically encoded FRET-based biosensor for Rac3. This biosensor was designed with high sensitivity based on monomeric fluorescent proteins in contrast to other designs using dimerizing fluorescent protein pairs (Reinhard et al., 2016; Rosenberg et al., 2017). Within the activation compartment of the membrane subdomains, dimerization effects could: (A) push toward elevated FRET through aggregation caused by reduced diffusive degrees of freedom or (B) bias the biosensor to a high FRET state because of an increased apparent on rate as a result of dimerization between the components within the biosensor. Indeed, previous results using a dimerizing biosensor pointed to ring localization of Rac3 activity at invadopodia but not in the core (Rosenberg et al., 2017). Our biosensor balanced the on versus off rates using monomeric fluorescent proteins and included autoinhibitory regulation of the binding domain affinity, allowing us to monitor the activity of Rac3 with excellent sensitivity. Using this biosensor, we found that two differentially regulated populations of active Rac3 are present at invadopodia. In the invadopod core, Rac3 activity oscillated at a similar rate as other core components, including cortactin and Tks5, observed both during 2D and 3D invasion (Magalhaes et al., 2011). The second population of active Rac3 exists in a ringlike compartment around the core. Importantly, this oscillation and changes in the location of Rac3 activity were not caused by changes in the bulk protein localization of Rac3, as we have never observed ringlike accumulation of Rac3 protein at invadopodia. Interestingly, the ringlike localization of Rac3 activity was more clearly observed when the data were subjected to a maximum projection over time. This indicates a temporally stochastic activation dynamic that eventually coalesces into a ringlike region similar to the RhoC activity that we have described previously in this location (Bravo-Cordero et al., 2011). Indeed, expression of the constitutively activated version of the Rac3 biosensor showed a more prominent ringlike Rac3 activity in the absence of such temporal projection methodology, pointing to the reversibility of the biosensor being critical to observing these highly transient activation patterns that regulate biological functions.

Our biosensor revealed that two GEFs, Vav2 and βPIX, together orchestrate the complex dynamics of Rac3 activity at invadopodia. We found that Vav2 regulates Rac3 activity in the core of invadopodia, whereas βPIX activates Rac3 only in the ringlike compartment. As depletion of either GEF does not affect Rac3 activity in the other compartment, this suggests independent mechanisms of upstream regulation. Recently, recruitment of activated Vav2 at the core of invadopodia was shown to be downstream of Arg kinase–mediated phosphorylation of cortactin (Rosenberg et al., 2017). Consistent with this, depletion of Rac3 had no effect on the phosphorylation of cortactin tyrosine-421 (not depicted), suggesting that the core-associated Vav2-Rac3-GIT1 axis is downstream of the Arg kinase pathway. However, βPIX is traditionally linked to adhesion signaling (Turner, 2000). This suggests that the ringlike compartment may also be adhesion dependent, which is consistent with previous observations of paxillin and other adhesion-associated molecules surrounding invadopodia cores (Branch et al., 2012). Thus, it is conceivable that localization of βPIX surrounding the invadopodia activates Rac3 in this ringlike region, promotes Rac3–GIT1 interaction, and potentially results in a positive feedback loop as GIT1 and βPIX also interact (Botrugno et al., 2006). This would stabilize the active βPIX–Rac3–GIT1 axis, resulting in sustained signaling to Arf6 GTPase. Although the function of this ringlike compartment remains unclear, several other molecules show similar localization. Previously, we found that activity of RhoC and its upstream activator p190RhoGEF also surround the core of the invadopodia (Bravo-Cordero et al., 2011). In a related study, the localization of p190RhoGEF was organized through interaction with focal adhesion kinase, which was required for the spatially distinct activation pattern of RhoC at the leading edge (Bravo-Cordero et al., 2013), further pointing to the likely requirement for correctly placing upstream GEF complex to sculpt the Rho GTPase activation dynamics within a subcellular compartment.

We found that localization of GIT1, the downstream target of Rac3, mirrors that of Rac3 activity and exhibits similar dynamics as the core oscillation of Rac3 activity. Our data suggest that collectively, these proteins regulate surface presentation of MT1-MMP at invadopodia. Future studies will investigate how changes in the localization of activated GIT1 could modulate

(E) The percentage of invadopodia with EGFP-GIT1 in MTLn3 cells after starvation and EGF stimulation for indicated times. Significance is shown relative to the relevant bar at 0 min. $n \geq 50$ from ≥15 cells per condition; three independent experiments. (F) Differential localization times of EGFP-GIT1 at the core or ring of invadopodia in MTLn3 cells. $n = 7$ invadopodia from ≥5 different cells pooled from three independent experiments. (G) The percentage of GIT1-positive (total, core, or ring localization) invadopodia in MTLn3 cells treated with control (black bars) or Rac3 siRNA (gray bars) plated on gelatin for 16 h. (H) The percentage of GIT1-positive (total, core, or ring localization) invadopodia in MTLn3 cells transfected with WT (black bars) or Rac3 T35S/Y40C effector binding mutant (gray bars) plated on gelatin for 16 h. (I) Normalized mean degradation area per field for cells overexpressing EGFP-GIT1 WT (black bars) or EGFP-GIT1-R39K (Arf-GAP deficient mutant). $n \geq 10$ fields for each condition; three independent experiments. (J) Percentage of invadopodia with cytoplasmic (internal) MT1-MMP or surface (external) MT1-MMP in cells treated with the indicated siRNA. Significance is shown relative to the relevant control bar. *, $P \leq 0.05$; **, $P \leq 0.01$; ***, $P \leq 0.001$. All error bars are SEM.

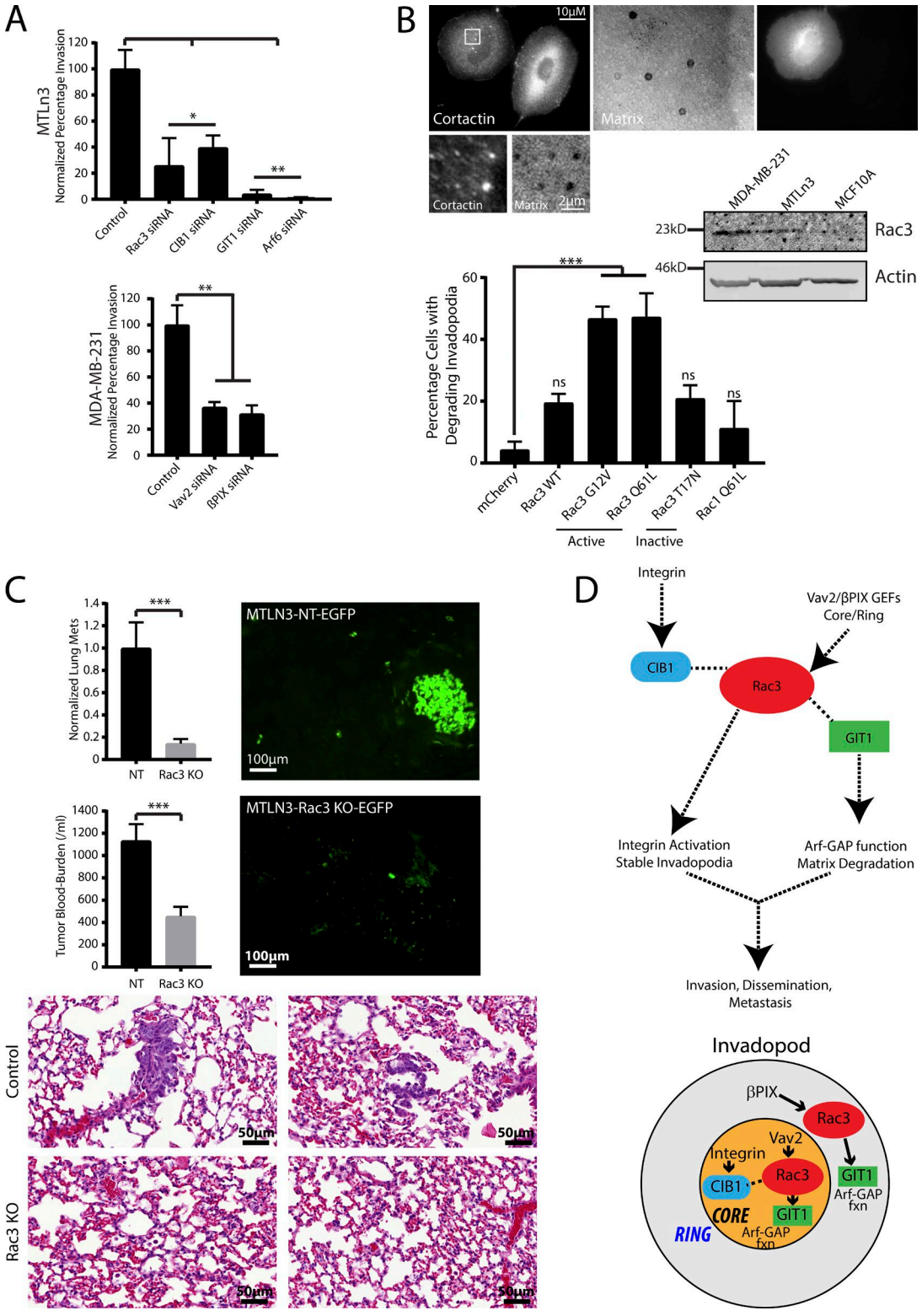

Figure 6. **Rac3 impacts invasion, dissemination, and metastasis.** (A) The percentage of invading cells in the in vitro invasion assay for cells with control, Rac3, CIB1, GIT1, Arf6, Vav2, or βPIX siRNA. $n \geq 900$ cells per condition; three independent experiments. (B) Representative image showing MCF10A cells transfected with Rac3 G12V mutant (left cell) or untransfected (right cell) plated on 405 nm fluorescent gelatin for 16 h. Zooms show invadopodia (cortactin colocalizing with spots of matrix degradation). (B, bottom) Quantification of the percentage of cells transfected with the indicated constructs that have at least one degrading invadopod (identified by the colocalization of cortactin, Tks5, and spots of matrix degradation). The Western blot shows Rac3 expression levels in lysates from the indicated cell lines. (C) Representative images of lung metastases in MTLn3 nontargeting (NT) control (top) or Rac3-knockout (KO) cells (bottom) expressing EGFP. (C, top) Normalized lung metastases in mice spontaneous metastasis assay with nontargeting control or Rac3-knockout MTLn3 cells. (C, middle) Number of circulating tumor cells in the blood of the same mice. $n = 9$ control or 16 Rac3-knockout tumor-bearing mice. A Mann-Whitney *U* test was used to determine significance. *, $P \leq 0.05$; **, $P \leq 0.01$; ***, $P < 0.001$. (C, bottom) Representative H&E-stained sections of lungs in control mice versus Rac3-knockout mice. (D) Model of the signaling axes centering on Rac3 addressed in this study. All error bars are SEM.

the membrane trafficking pathways that target MT1-MMP delivery to invadopodia (Hashimoto et al., 2004; Sakurai-Yageta et al., 2008; Yu et al., 2012; Monteiro et al., 2013; Marchesin et al., 2015). Interestingly, the exocyst complex docks at invadopodia from the lateral aspect of the core (Monteiro et al., 2013), potentially coinciding with the ringlike localization of the βPIX–Rac3–GIT1 axis. Thus, it would be interesting to see whether the Arf-GAP function of GIT1, specifically in this ringlike region around invadopodia, is important to drive the vesicular trafficking at this location to enhance the surface presentation of MT1-MMP through efficient exo/endocytic cycling. To this end, additional work is needed to understand the spatial regulation of membrane recycling mediated by Arf6 GTPase (Marchesin et al., 2015). In light of the fact that invadopodial membrane is recycled within a specialized proinvasive compartment (Frittoli et al., 2014; Hagedorn et al., 2014), it is possible that Arf6 at invadopodia could have dual functions in recycling both the invadopodial membrane at the core and the plasma membrane at the ring to direct invadopodia maintenance as well as the delivery of MT1-MMP and the exocyst complex to invadopodia. These dual functions could be differentially mediated by Vav2–Rac3–GIT1–Arf-GTPase axis at the core of invadopodia to direct invadopodial membrane recycling and maintenance as well as βPIX–Rac3–GIT1–Arf-GTPase in the regions around invadopodia to direct exocyst complex function.

Ultimately, we linked our molecular analyses of Rac3 in balancing ECM adhesion and ECM degradation to a functional role in a mouse model of breast adenocarcinoma metastasis. We show that genetic deletion of Rac3 significantly impacts lung metastasis in the orthotopic metastasis assay in mice. Our data demonstrate that this is likely through defects in invasion and intravasation, which are important during the early phases of the metastatic cascade. In summary, we show that Rac3 is a critical signaling node that regulates the balance of ECM adhesion and ECM degradation, which is required for efficient invasion of breast tumor cells during the metastatic cascade.

Materials and methods

Cell culture

MTLn3 cells were cultured in MEM supplemented with 5% FBS, 1% glutamine, and penicillin/streptomycin (Invitrogen) as previously described (Neri and Nicolson, 1981). Transfections were performed as follows using Lipofectamine 2000 (Invitrogen). Cells were plated at 2×10^5 cells/well of a six-well plate. The next day, 2 µg of DNA was added to 250 µl of Opti-MEM and vortexed. 4 µl of Lipofectamine 2000 was added to 250 µl of Opti-MEM, vortexed, and then incubated at room temperature for 5 min. The Lipofectamine solution was then added to the DNA mixture, vortexed, and incubated for 20 min at room temperature. In this time, cells were washed once with PBS, and then 500 µl of Opti-MEM was added to the well. Transfection mixture was added, and the media were replaced with normal culture medium 45 min later. MDA–MB-231 (HTB-26; ATCC) cells were cultured in DMEM supplemented with 10% FBS, 1% glutamine, and penicillin/streptomycin (Invitrogen). MCF10A (CRL 10317; ATCC) cells were cultured following the ATCC protocols. MCF10A cells were transfected with Lipofectamine 2000 using the same protocol as for MTLn3 cells (Ioannou et al., 2015). MDA–MB-231 cells were transfected either by nucleofection according to manufacturer's protocols (Lonza) or using Lipofectamine 2000 using the same protocol as for MTLn3 cells. All cell lines were mycoplasma tested.

Degradation assays

Atto-680 NHS Ester (Sigma-Aldrich) or Alexa Fluor 405 NHS Ester (Thermo Fisher Scientific) were conjugated to 0.2% porcine gelatin (Sigma-Aldrich) according to the manufacturer's protocols. 35-mm glass-bottom MatTek dishes (MatTek Corporation) were coated with a thin gelatin layer as previously described (Chen, 1989). In brief, dishes were coated with poly-L-lysine (50 µg/ml) for 20 min, washed three times with PBS, and then incubated with a prewarmed (37°C) 0.2% solution of gelatin (Sigma-Aldrich) dissolved in PBS for 10 min. Dishes were again washed three times in PBS before cross-linking with a 0.2% (0.02% for MDA–MB-231 cells) solution of glutaraldehyde followed by quenching with a 5 mg/ml solution of sodium borohydride (Sigma-Aldrich). Before plating cells, dishes were incubated in normal culture medium for at least 20 min. Cells were plated at a density of 10^5 on these dishes for 16 h (MTLn3 and MCF10A) or 4 h (MDA–MB-231) before fixation in 3.7% PFA. Gelatin degradation was measured by quantifying the mean area of nonfluorescent pixels per field using a manual threshold in ImageJ (National Institutes of Health).10–15 random fields were imaged per condition, and each independent experiment was performed at least three times and averaged. For rescue experiments, only the degradation area underneath transfected cells was quantified. Invadopodia were identified by costaining with Cortactin (mouse; ab33333; Abcam) and Tks5 (rabbit; M-300 [Santa Cruz Biotechnology, Inc.] or 09-403 [EMD Millipore]) antibodies and then were manually counted from images.

EGF stimulation

EGF stimulation was performed as previously described (Bravo-Cordero et al., 2011; Moshfegh et al., 2014). In brief, MTLn3 cells were starved for 3 h in L15 media containing 0.00345% BSA at 37°C (without CO_2) and then stimulated with 5 nM EGF (53003-018; Invitrogen) for the indicated times before fixing with 3.7% PFA. Stimulations were performed at 37°C.

Pulldown experiments

HEK293T cells were plated at a density of 10^6 cells on poly-L-lysine–coated six-well plates. The next day, the cells were transfected using Lipofectamine 2000 according to the manufacturer's protocols. 24 h later, cells were lysed in a buffer containing 1% NP-40, 20 mM Tris, pH 7.5, 150 mM NaCl, 10 mM imidazole, pH 8.0, 1 mM PMSF, and protease inhibitors. Lysates were clarified by centrifugation at 14,000 rpm for 10 min at 4°C. After removing an "input" fraction, lysates were incubated with washed COBALT resin overnight at 4°C with rotation. Samples were washed 3× in lysis buffer, resuspended in final sample buffer, and analyzed by Western blotting. Biosensor pulldowns using purified PAK1-PBD-agarose beads were performed as previously described (Moshfegh et al., 2014). To prepare the glutathione (GSH)-agarose beads, 72 mg of GSH-agarose (Sigma-Aldrich) was resuspended into 10 ml of sterile water and incubated at 4°C for 1 h. The suspension was briefly centrifuged, and the pellet was washed three times with sterile water followed by washing twice in resuspension buffer (50 mM Tris, pH 8.0, 40 mM EDTA, and 25% sucrose). The washed GSH-agarose slurry was resuspended in 1 ml of resuspension buffer. To produce GST-PAK1-PBD, pGEX-PBD (a gift from G. Bokoch; Benard and Bokoch, 2002) was transformed into BL21DE3-competent bacteria (Agilent Technologies) and grown in a shaker flask at 225 rpm and 37°C until it reached the optical density of 1.0 at 600 nm. Protein synthesis was induced by addition of IPTG at 0.2 mM and then immediately chilled to room temperature and allowed to incubate in a shaker flask at 225 rpm and 24°C overnight. The next day, bacteria were pelleted and resuspended in 20 ml of resuspension buffer containing 1 mM PMSF, protease inhibitor cocktail (Sigma-Aldrich), and 2 mM

β–mercaptoethanol and rotated on a Nutator for 20 min at 4°C. After the incubation, 8 ml of detergent buffer (50 mM Tris, pH 8.0, 100 mM $MgCl_2$, and 0.2% [wt/vol] Triton X-100) was added, and the mixture was incubated at 4°C for 10 min on a Nutator. After the incubation, the mixture was ultrasonicated (4× cycle of 30-s ultrasonication followed by 1 min rest on ice) and centrifuged at 22,000 *g* for 45 min at 4°C. The supernatant was transferred to a 50-ml tube, and 1 ml of GSH-agarose beads as prepared earlier was added and incubated at 4°C for 1 h on a Nutator. The beads were then pelleted by a brief centrifugation and washed four times with the wash buffer (50 mM Tris, pH 7.6, 50 mM NaCl, and 5 mM $MgCl_2$) followed by resuspension into 500 µl of 50:50 glycerol/wash buffer, and 50 µl aliquots of this mixture was frozen at −80°C for storage. For pulldown experiments, HEK293T cells were transfected and lysed as above. Lysates were clarified by centrifugation at 14,000 rpm for 10 min at 4°C. After removing an "input" fraction, lysates were incubated with PAK1-PBD–conjugated agarose beads for 1 h at 4°C, washed 3× in lysis buffer, resuspended in final sample buffer, and analyzed by Western blotting. Incubation with Ponceau S solution (Sigma-Aldrich) was used to visualize GST–PAK1-PBD to control for equal loading. Anti-GFP (mouse; 11814460001; clones 7.1 and 13.1 mix; Roche) antibody was used to detect the Rac3 biosensor or fluorescently tagged Rac3 protein.

Western blotting

Cell lysates were resolved on 10% or 12% SDS-polyacrylamide gels. Proteins were transferred to polyvinylidene fluoride membranes. Primary antibody incubations were done overnight at 4°C at 1:1,000 dilution. Secondary fluorescently conjugated antibodies (LI-COR Biosciences) were diluted 1:10,000 and incubated for 1 h at room temperature. Immunoblots were visualized using the Odyssey Imager (LI-COR Biosciences).

Invadopod lifetime

An invadopod lifetime assay was performed as previously described (Moshfegh et al., 2014). In brief, MTLn3 cells were transfected with cortactin-mTagRFP and Tks5-EGFP before plating on gelatin-coated coverslips for 16 h. Imaging was performed on a widefield epifluorescence microscope (see the Microscopy imaging section), and cells were imaged every 2 min for 4 h. Invadopod lifetime was manually quantified for at least 20 invadopodia in a minimum of five cells per condition for three independent experiments. Control and siRNA conditions were imaged on the same day for each independent experiment. For experiments overexpressing mCherry-Rac3, invadopodia lifetimes were quantified and categorized according to whether they recruited Rac3 at any point during their lifetime. For Mn^{2+} experiments, Rac3-depleted MDA–MB-231 cells were plated on gelatin-coated coverslips for 2 h before incubation with 5 mM Mn^{2+} (Theodosiou et al., 2016) for 45 min before the initiation of imaging. Cells were imaged every 2 min for 3 h with Mn^{2+} in the media. Residence time of EGFP-GIT1 in the core or ring of invadopodia was manually counted from time-lapse videos in which cells were imaged every 2 min for at least 4 h.

In vitro invasion assays

In vitro invasion assays were performed as previously described (Bravo-Cordero et al., 2011). In brief, 5×10^5 cells were suspended in low (0.25%)-serum culture medium and plated in duplicate in the top well of growth factor–reduced Matrigel-coated invasion chambers (8-µm pore size; BD BioCoat; 354483; BD). Normal serum-containing media (5% serum) were placed in the lower chamber, and cells were allowed to invade for 24 h at 37°C. (For MDA–MB-231 cells, the low-serum culture media contained 0.5% serum, whereas normal growth media contained 10% serum.) The assay was fixed with 3.7% PFA for 20 min and then stained with DAPI or NucBlue Live Cell Stain ReadyProbes reagent (R37605; Molecular Probes) to visualize nuclei. Four to six random fields were acquired at 20× magnification on an SP5 confocal microscope (Leica Microsystems). The number of invaded cells was counted manually with ImageJ software and normalized to the total number of cells present in the insert. Data are means of three independent experiments for each condition.

Reagents

Cortactin–mtagRFP-T (Oser et al., 2009) and Tks5-EGFP (Courtneidge, 2012) have been previously described. To generate cortactin-miRFP703, mTag-RFP was replaced with miRFP703 (Shcherbakova et al., 2016). Cortactin antibodies were purchased from Abcam (mouse; clone 0.T.21; used at 1:600; ab3333) and Santa Cruz Biotechnology, Inc. (goat polyclonal; G-18). Rac3 (07-2151 polyclonal for immunofluorescence) antibody was purchased from EMD Millipore; Rac3 (rabbit, ab129062 for Western blotting) antibody was purchased from Abcam. β-Actin (mouse; clone AC-15; sc-69879; Santa Cruz Biotechnology, Inc.), βPIX (rabbit; 07-1450-I; EMD Millipore), and Vav2 (rabbit; H-200; Santa Cruz Biotechnology, Inc.) were also used. The GFP antibody was purchased from Roche (mouse; clones 7.1 and 13.1 mix; 11814460001). Unless stated, all primary antibodies were used at 1:200 dilution for immunofluorescence and 1:1,000 for Western blotting. Additionally, the following antibodies were used: RhoA (mouse; 26C4; sc-418; Santa Cruz Biotechnology, Inc.), Cdc42 (rabbit; 1:200 Western blot; P1; sc-87; Santa Cruz Biotechnology, Inc.), Rac1 (mouse; clone 23A8; EMD Millipore), GIT1 (mouse; transduction 611396; BD), polyclonal MT1-MMP (rabbit; AB6004; EMD Millipore), monoclonal MT1-MMP (mouse; clone LEM-2/15.8; MAB3328; EMD Millipore), Arf6 (mouse; 3A-1; Santa Cruz Biotechnology, Inc.), CIB1 (mouse; clone 3C5; MAB2601; EMD Millipore), total integrin β1 (mouse; P5D2; sc-13590; Santa Cruz Biotechnology, Inc.), active integrin (9EG7), and rat anti–mouse CD29 (550531; BD). MT1-MMP–GFP was as previously described (Bravo-Cordero et al., 2007). pEGFP-GIT1 was a gift from R. Horwitz (Allen Institute for Cell Science, Seattle, WA; 15226; Addgene). GIT1-R39K was generated using the QuikChange mutagenesis kit (Agilent Technologies). WT Rac3 was purchased from cdna.org. Activating and inactivating mutations were generated using the QuikChange mutagenesis kit (Agilent Technologies; see the Mutagenesis primers section for primers used). Rac1 and Rac3 were cloned into pTriEX-His-Myc-4 backbone (Novagen) at EcoRI and XhoI sites for protein expression. pcDNA3.1-CIB1-Myc was a gift from J. Groffen and N. Heisterkamp (Children's Hospital Los Angeles, Los Angeles, CA, and University of Southern California, Riverside, CA; 32505; Addgene). It was cloned into pEGFP-N1 using the EcoRI and KpnI sites. pEGFP-Vav2 was derived from pC.HA Vav2, which was a gift from J. Brugge (14554; Addgene; Moores et al., 2000). pEGFP-βPIX was a gift from P. Hordijk (University Medical Center, Amsterdam, Netherlands).

Primers used

Primers used in this study can be found in Table 1.

RNAi

siRNA SMARTpools for Rac3 (Human L-008836 and rat M-114657); GIT1 (M-088071-01); CIB1 (M-096735-01); Vav2 (M-005199-02); βPIX (M-009616-00); and Arf6 (M-096951-01) were purchased from GE Healthcare. Individual oligonucleotides for Rac3 (LU-008836) were also purchased from GE Healthcare. Transfections were performed with Oligofectamine (Invitrogen) for MTLn3 cells or electroporated using Amaxa Cell Line nucleofector kit V (VACA-1003; Lonza) for MDA–MB-231 cells following the manufacturers' protocols. Knockdown was assessed and subsequent assays were performed at 48 h

(MTLn3) or 72 h (MDA–MB-231) after transfection. Quantification of knockdown efficiencies was performed using ImageJ.

Generation of Rac3-knockout cell line using CRISPR/Cas9

Four different 20-nt guide sequences for Rac3 were selected using the online CRISPR Design Tool (http://tools.genome-engineering.org). Sequences for primer pairs are as follows: single-guide RNA (sgRNA) 1, 5′-CACCGAGAACCGATCTCTCGGGCCA-3′ and 5′-AAACTG GCCCGAGAGATCGGTTCTC-3′; sgRNA 2, 5′-CACCGGGACACA ATTGAACGGCTGC-3′ and 5′-AAACGCAGCCGTTCAATTGTG TCCC-3′; sgRNA 3, 5′-CACCGACTTGACAGAACCGATCTCT-3′ and 5′-AAACAGAGATCGGTTCTGTCAAGTC-3′; and sgRNA 4, 5′-CACCGGGCAGTGGTGCCGCACCTCT-3′ and 5′-AAACAGAGG TGCGGCACCACTGCCC-3′.

A negative control NT1 of sequence 5′-GCGAGGTATTCGGCT CCGCG-3′ was also used. This was derived from a negative control sequence pulled from the GeCKOv2 Mouse Library Pool A (Shalem et al., 2014). sgRNAs were cloned into the lentiCRISPR v2 plasmid (Sanjana et al., 2014; Shalem et al., 2014) by digestion with BsmBI (Esp3I; ER0451; Thermo Fisher Scientific). lentiCRISPR v2 was a gift from F. Zhang (Massachusetts Institute of Technology, Cambridge, MA; 52961; Addgene) The GP2-293 cell line (Takara Bio Inc.) was used to produce lentivirus by cotransfecting the pVSVg, gag-pol, rev, and tat vectors (Takara Bio Inc.). MTLn3 cells were infected with the lentivirus containing the four sgRNAs or NT1 control sgRNA and were cultured as described in the Cell culture section. They were selected for stable incorporation of the CRISPR/Cas9 vector by puromycin treatment (2 µg/ml). CRISPR knockout efficiency was assessed by Western blotting for Rac3 (Fig. S5 A). Successful knockout was achieved with sgRNA2 and sgRNA4, and we proceeded to use sgRNA2 cells in subsequent experiments.

Rac3 biosensor

The previously published and optimized single-chain FRET biosensor for Rac1 (Moshfegh et al., 2014; Miskolci et al., 2016) was used as the backbone for the Rac3 biosensor. In brief, the optimized biosensor backbone contained a monomeric Cerulean1 (mCer1) as the FRET donor as well as two tandem PBDs of p21-activated kinase 1 (PAK1; amino acid residues 70–149) to achieve autoinhibitory regulation, separated by the structurally optimized linker (5′-GSGGPPGSGGSG-3′) monomeric circularly permutated-229 Venus (mcp229Ven) as a FRET acceptor as well as a full-length WT Rac3. The second PBD contained H83D and H86D point mutations to render it unable to bind to active GTPase. Furthermore, the final version of the Rac3 biosensor also contained an additional linker optimization applied to mcp229Ven by replacing the first 16 amino acids with a flexible, structureless linker that is resistant to protease cleavage (Whitlow et al., 1993). Rac1 was replaced by a full-length WT Rac3, PCR-amplified using the primer pair 5′-CCTTATATGCATTGTTATATGAATTCATGCAGGCCATCA AGTGCGTGGTGG-3′ and 5′-CGATTAAATATACGCAATATCTCG AGTTACTAGAAGACGGTGCACTTCTTCCCC-3′, and then was subcloned into the biosensor backbone using the EcoRI and XhoI restriction sites. The synonymous modifications (Wu et al., 2015) were applied to the mCer1 and the second PBD as in the original Rac1 biosensor. The resulting biosensor construct was cloned into a pTriEX-4 backbone (Novagen) at NcoI–XhoI sites. The QuikChange mutagenesis kit (Agilent Technologies) was used to introduce point mutations into the fragment encoding the Rac3 GTPase, producing different mutant versions of the biosensor.

Mutagenesis primers

Mutagenic primers used in this study can be found in Table 2.

Table 1. **Primers used in this study.**

Primer	Sequence
CIB-GFP EcoR1 forward	gatccgacttatgaattctgccaccatgggggctcggg cagtcgcctg
CIB-GFP Kpn1 reverse	ataagtcggatcggtaccttcaggacaatcttaaaggagctggc
GIT1 R39K forward	gtgctgcagcgtgcacaagagcctgggacgccac
GIT1 R39K reverse	gtggcgtcccaggctcttgtgcacgctgcagcac
Vav2 EcoR1 forward	attattattgaattcgccaccatggagcagtggcggcagtg
Vav2 Kpn1 reverse	ttattattaggtacccccctggatgccctcctcttctac

Fluorometric characterization and validation

Characterization of biosensor response was performed in HEK293T cells by transiently overexpressing WT or mutant versions of the biosensor with or without the appropriate upstream regulators as described previously (Pertz et al., 2006; Hodgson et al., 2008). In brief, HEK293T cells were plated overnight at 1.25×10^6 cells/well of six-well plates coated with poly-L-lysine (Sigma-Aldrich) and then transfected the next day using Lipofectamine 2000 reagent (Invitrogen) according to the manufacturer's protocols. Biosensors were cotransfected at ratios of 1:2 with GDI or 1:3 with GAP or 1:0.5–10 for cotransfection with GEFs (±GDI) as indicated. Adherent cells were washed in PBS and fixed using 3.7% formaldehyde 48 h after the transfection, and fluorescence emission spectra were measured with a spectrofluorometer using a plate reader (Horiba-Jobin-Yvon Fluorolog-3MF2 and MicroMax plate reader attachment; HORIBA). The fluorescence emission spectra were obtained by exciting the specimen at 433-nm wavelength light, and emission fluorescence was scanned between 450–600 nm. The background fluorescence reading of cells containing an empty vector (pCDNA3.1) was used to measure light scatter and autofluorescence and was subtracted from the data. The resulting spectra were normalized to the peak mCer1 emission intensity at 474 nm to generate the final ratiometric spectra.

To validate the biosensor in cancer cells using exogenous stimulation, MTLn3 cells transiently expressing the biosensor were serum starved for 3 h and stimulated using medium containing 5% serum. Cells were fixed and imaged at 0, 3, and 10 min after stimulation and analyzed for FRET change.

Microscopy imaging

MDA–MB-231 cells were plated at 2×10^5 cells per well the day before transfection. The cells were cotransfected with cortactin-mtagRFP and the Rac3 biosensor using Lipofectamine 2000 (Invitrogen) according to the manufacturer's protocol. The next day, cells were replated on unlabeled gelatin. Cells were time-lapse imaged beginning 2–3 h after plating. Coverslips were cleaned by ultrasonication followed by soaking in 100% ethanol before use in these studies and coated with gelatin as described in the Degradation assays section (Bravo-Cordero et al., 2011; Moshfegh et al., 2014). Cells were imaged in Ham's F-12K medium without phenol red (Crystalgen), sparged with argon gas to remove dissolved oxygen, and supplemented with 5% FBS, 10 mM Hepes, Oxyfluor reagent (1:100 dilution; Oxyrase Inc.), and 10 mM dl-lactate (Sigma-Aldrich). Cells were imaged at 37°C in a closed chamber mounted on a microscope stage. For fixed imaging, cells were fixed for 20 min with 3.7% PFA/PBS at 6 h after plating on gelatin and processed for immunofluorescence. We used the standard widefield microscopy, TIRF microscopy, and image deconvolution (3D blind-

Table 2. **Mutagenic primers used in this study.**

Primer	Sequence
Rac3 G12V forward	ggtcggcgacgtcgccgtgggga
Rac3 G12V reverse	tccccacggcgacgtcgccgacc
Rac3 T17N forward	gacggcgccgtggggaagaattgcttgctgatc
Rac3 T17N reverse	gatcagcaagcaattcttccccacggcgccgtc
Rac3 Q61L forward	ggacacagcgggtctggaggactacgatc
Rac3 Q61L reverse	gatcgtagtcctccagacccgctgtgtcc
Rac3 T35S forward	cccggagagtacatccccagcgtttttgacaac
Rac3 T35S reverse	gttgtcaaaaacgctggggatgtactctccggg
Rac3 Y40C forward	caccgtttttgacaactgctctgccaacgtgatgg
Rac3 Y40C reverse	ccatcacgttggcagagcagttgtcaaaaacggtg

iterative algorithm was used; Microvolution, LLC) in our fluorescence microscopy experiments.

Rac3 activity was measured in cells using an IX81-ZDC microscope (Olympus) with TIRF modality. For live-cell imaging, images were acquired through a 60× magnification objective lens (UIS 60× 1.45 NA TIRF; Olympus) using a custom microscope (Spiering and Hodgson, 2012) capable of simultaneous acquisition of FRET and mCerulean emissions through two Coolsnap ES2 cameras (Photometrics) mounted via an optical beam splitter and containing a T505LPXR mirror, ET480/40M for mCerulean emission, and ET535/30M for mVenus-FRET emission (Chroma Technology Corp). Relative intensities between the two channels were balanced by inclusion of a neutral density filter (ND0.2) so that the range of brightness in both mCerulean and FRET channels were similar to each other. Cells were illuminated by a 442-nm solid-state diode laser (SpectraPhysics) attached to a single-line TIRF module (Olympus) and were combined with the mercury arc lamp–sourced excitation light via ZT442dcrb-UF3 custom notch-dichroic mirror (Chroma Technology Corp). This arrangement allowed for TIRF modality imaging of mCerulean and FRET channels as well as epifluorescence acquisitions of other wavelengths as required. Metamorph (7.8.13; Molecular Devices) was used to perform the image acquisition. Metamorph and MatLab (Mathworks) were used to perform image processing and data analysis. Image processing included camera noise subtraction, flatfield correction, background subtraction, image registration, ratio calculations, and correction for photobleaching (Spiering et al., 2013). In brief, camera noise images were acquired at the same exposure times as the foreground image sets but without the field illumination. This represented the camera read noise and the dark current noise and was subtracted from all subsequent foreground images. Flatfield correction involved acquisition of cell-free fields of view with the same exposure and field illumination conditions as the foreground image sets and then camera noise subtracted to obtain the shading images. The camera noise–subtracted foreground images were then divided by the shading images to obtain flatfield-corrected images. A small region of interest in the background (cell-free) area was selected in the flatfield-corrected foreground image sets, and the mean gray value from such a region was subtracted from the whole field of view, calculated, and processed at each time point to result in the background-subtracted image sets. The background-subtracted image sets were then subjected to an *affine* transformation based on a priori calibration to account for misalignments between the two cameras used for the simultaneous imaging of the FRET and the mCerulean channels. After the transformation, a linear X–Y registration was performed on the two resulting image sets before ratio calculations where the FRET image set was divided by the mCerulean channel image set. For photobleach correction of the ratio image set, whole-cell mean gray values were calculated at each time point and fitted to a biexponential decay model. The inverse function of the regressed model was then multiplied into the ratio image set to approximate for the effect of photobleaching. For fixed-cell biosensor imaging, a single Coolsnap HQ2 camera (Photometrics) attached on the bottom port of the microscope was used together with a 60× magnification objective lens. In this case, excitation and emission filter wheels switched appropriate filter sets in addition to the laser light source to acquire mCerulean, mVenus, and FRET emissions plus any other additional wavelengths as required. For imaging of biosensors, we adjusted the camera acquisition time duration by targeting to fill ∼80% of the total digitization range of the charge-coupled device circuitry to maximize the dynamic range, using excitation intensities of 0.4–1.0 mW at the specimen plane.

Analysis of integrin staining at invadopodia

A region was created in Metamorph that encompassed a single invadopod. Invadopodia were identified using costaining of cortactin and Tks5, and then the mean fluorescence intensity in the active or total integrin images was measured using the region described above. A ratio of active over total integrin was taken for each invadopodia.

Rac3 activity analysis at invadopodia

A binary mask was created in Metamorph using cortactin fluorescence intensity as a reference to designate the core of the invadopodium. Subsequently, this mask was dilated 8 pixels, and the original core was subtracted to result in a binary mask designating the invadopodial ringlike region surrounding the core. These binary masks were used to measure the intensity in each compartment of the invadopodium. The area of the ring was based on spatial distance of 1.74-µm radius outside of the core, which is similar to the binary mask used in a previous work (Bravo-Cordero et al., 2011). A ratio of FRET intensity in the core/ring was calculated. To determine the threshold of an invadopodium that contains high core activity versus high ring activity, the SD of the core/ring ratio of the population of invadopodia was calculated. Invadopodia were designated as having high core Rac3 activity if the core/ring ratio was $\geq$1.0 + 1 SD. Conversely, invadopodia were designated as having high ring Rac3 activity if the core/ring ratio was $\leq$1.0 − 1 SD.

Maximum-intensity projections were created from at least 20 frames of time-lapse videos for Rac3 activity and cortactin-mtagRFP. Videos were acquired at a rate of one frame per min for at least 1 h. Linescan analysis of maximum-intensity projections was performed in Metamorph. 3.2-µm linescans were measured for each maximum-intensity projection using both vertical and horizontal lines passing through the center of the invadopodium (designated by maximum cortactin intensity). Linescans were normalized to 1.0 at the minimal center value (Rac3 activity) or the maximal center value (cortactin). The fluorescence datasets were aligned to the maximal center value position of cortactin fluorescence to represent the center of the invadopodia cores.

Autocorrelation analysis for periodicity

To quantitatively determine the periodicity of biosensor activity fluctuations within the core of an invadopodium versus the ring surrounding the invadopodium, the time series of the ratio of intensities measured within binary masks created to target the core of invadopodium versus the ring surrounding the invadopodium core were analyzed using the autocorrelation function *xcov* in MatLab. The individual autocorrelation function distribution was smooth-spline fitted, pooled between all invadopodia analyzed in all cells imaged and the mean autocorrelation function, and the 95% confidence intervals were calculated by a nonparametric bootstrap method (Efron and Tibshirani, 1993). The measured temporal width to the peaks of the first side lobes after the zero-crossing was taken as the period of oscillation (Machacek et al., 2009).

Analysis of tumor intravasation and metastasis in vivo

MTLn3 cells stably expressing EGFP and containing Rac3 deletion via CRISPR/Cas9 were injected into the mammary gland of female severe combined immune deficiency mice (6–8 wk old; Jackson ImmunoResearch Laboratories, Inc.; Zhou et al., 2014). 1.0×10^6 cells were trypsinized and resuspended in 100 µl of PBS per mouse for the injection. (Total number of mice injected: CRISPR/Cas9 nontargeting control, $n = 20$ mice; Rac3-knockout mice, $n = 20$ mice). Mice were sacrificed 3–4 wk after injection when the primary tumor had reached 1 cm in diameter. Lung metastases were confirmed and counted at necropsy using a fluorescent microscope to image EGFP fluorescence. Randomly selected 12 fields of view at 10× magnification per mouse lung (six fields of view per lung lobe) were analyzed for the total EGFP fluorescence area ratio to the background area. To quantify the circulating tumor cell counts, 1 ml of mouse blood obtained through cardiopuncture at the time of euthanasia was lysed in red blood cell lysis buffer (04-4300-54; Thermo Fisher Scientific/eBioscience) according to the manufacturer's protocols. The remaining cells were plated into MTLn3 growth media and cultured for one additional week. The numbers of EGFP-positive MTLn3 cells were quantified by counting 1/4 of the area of 10-cm tissue culture dishes per animal. All animal experiments were performed in accordance with an approved protocol by the Office of the Institutional Animal Care and Use Committee of the Albert Einstein College of Medicine (protocol 20140415). For data analysis, mice with primary tumors that showed indications of ulceration or intraperitoneal growths were omitted from the final tally. Lung samples were fixed in 10% neutral formalin buffer and then sent to the Einstein Histopathology Core, where they were paraffin embedded, sectioned, and stained with H&E.

Statistical analysis

The two-tailed Student's *t* test was used to determine the p-values for all experiments unless otherwise stated. In experiments where more than two samples were compared, an ordinary one-way ANOVA was used with a Tukey multiple comparison test. No randomizations were used. The investigators were not blinded to allocation during experiments and outcome assessment. Data distribution should meet the normal distribution requirements. In animal experiments, data distribution was not assumed a priori to be normal distribution; therefore, the Mann-Whitney *U* test was used. No estimate of variation. No preestablished criteria were used to determine data inclusion/exclusion.

To determine the required numbers of animals for the metastasis and intravasation assays, we estimated that at least 15 animals for the metastasis and intravasation assays would provide >84% study power to detect a 2.2-fold increase or decrease between experimental conditions at a two-sided α level of 0.05, as previously described (Wang et al., 2003).

Online supplemental material

Fig. S1 shows the specificity of Rac3 antibody. Fig. S2 shows how Rac3 is enriched at invadopodia and required for matrix degradation. Fig. S3 shows how a Rac3 FRET biosensor reveals two spatially distinct pools of Rac3 activity at invadopodia. Fig. S4 shows how Rac3 targets GIT1 to regulate MT1-MMP–mediated matrix degradation at invadopodia. Fig. S5 shows CRISPR/Cas9 genetic editing of Rac3. Video 1 shows invadopodia lifetimes in control cells. Video 2 shows how invadopodia lifetimes are significantly reduced when Rac3 is depleted. Video 3 shows how invadopodia lifetimes are significantly reduced when CIB1 is depleted. Video 4 shows how GIT1 oscillates between invadopodia core and the ring.

Acknowledgments

We thank members of the Condeelis, Segall, and Cox laboratories for their helpful discussions.

This work was supported by American Cancer Society Lee National Denim Day Postdoctoral Fellowship PF-15-135-01-CSM (S.K. Donnelly); National Institutes of Health grants K22CA196750 (J.J. Bravo-Cordero), CA100324 (J.E. Segall and J.S. Condeelis), CA150344 (J.S. Condeelis), T32GM007491 (J.R. Christin), T32GM007288 (R. Cabrera and S.P.H. Mao), and CA205262 (L. Hodgson); and the Tisch Cancer Institute Young Scientist Cancer Research Award Joshua and Julia Ruch Foundation Fund P30 CA196521 (J.J. Bravo-Cordero). W. Guo is a V Foundation for Cancer Research V Scholar. J.R. Christin received a New York State Department of Health – Wadsworth Center NYSTEM training grant C30392GG.

The authors declare no competing financial interests.

Author contributions: S.K. Donnelly and L. Hodgson conceived the project. S.K. Donnelly performed the majority of the experiments. R. Cabrera, S.P.H. Mao, and J.E. Segall helped design and perform the mouse experiments. J.R. Christin and W. Guo gave technical advice on the CRISPR experiments. J.J. Bravo-Cordero made initial experimental observations and gave technical advice on experimental methods. B. Wu advised on methods of lentiviral transduction. J.S. Condeelis and J.E. Segall gave critical feedback. S.K. Donnelly and L. Hodgson wrote and revised the manuscript. All authors gave feedback on the manuscript.

Submitted: 6 April 2017
Revised: 28 July 2017
Accepted: 25 September 2017

References

Abe, K., K.L. Rossman, B. Liu, K.D. Ritola, D. Chiang, S.L. Campbell, K. Burridge, and C.J. Der. 2000. Vav2 is an activator of Cdc42, Rac1, and RhoA. *J. Biol. Chem.* 275:10141–10149. https://doi.org/10.1074/jbc.275.14.10141

Artym, V.V., Y. Zhang, F. Seillier-Moiseiwitsch, K.M. Yamada, and S.C. Mueller. 2006. Dynamic interactions of cortactin and membrane type 1 matrix metalloproteinase at invadopodia: defining the stages of invadopodia formation and function. *Cancer Res.* 66:3034–3043. https://doi.org/10.1158/0008-5472.CAN-05-2177

Ayala, I., M. Baldassarre, G. Caldieri, and R. Buccione. 2006. Invadopodia: a guided tour. *Eur. J. Cell Biol.* 85:159–164. https://doi.org/10.1016/j.ejcb.2005.09.005

Baugher, P.J., L. Krishnamoorthy, J.E. Price, and S.F. Dharmawardhane. 2005. Rac1 and Rac3 isoform activation is involved in the invasive and metastatic phenotype of human breast cancer cells. *Breast Cancer Res.* 7:R965–R974. https://doi.org/10.1186/bcr1329

Beaty, B.T., and J. Condeelis. 2014. Digging a little deeper: the stages of invadopodium formation and maturation. *Eur. J. Cell Biol.* 93:438–444. https://doi.org/10.1016/j.ejcb.2014.07.003

Beaty, B.T., V.P. Sharma, J.J. Bravo-Cordero, M.A. Simpson, R.J. Eddy, A.J. Koleske, and J. Condeelis. 2013. beta1 integrin regulates Arg to promote invadopodial maturation and matrix degradation. *Mol. Biol. Cell.* 24:1661–1675.

Benard, V., and G.M. Bokoch. 2002. Assay of Cdc42, Rac, and Rho GTPase activation by affinity methods. *Methods Enzymol.* 345:349–359. https://doi.org/10.1016/S0076-6879(02)45028-8

Bergman, A., J.S. Condeelis, and B. Gligorijevic. 2014. Invadopodia in context. *Cell Adhes. Migr.* 8:273–279. https://doi.org/10.4161/cam.28349

Botrugno, O.A., S. Paris, L. Za, S. Gualdoni, A. Cattaneo, A. Bachi, and I. de Curtis. 2006. Characterization of the endogenous GIT1-betaPIX complex, and identification of its association to membranes. *Eur. J. Cell Biol.* 85:35–46. https://doi.org/10.1016/j.ejcb.2005.09.018

Branch, K.M., D. Hoshino, and A.M. Weaver. 2012. Adhesion rings surround invadopodia and promote maturation. *Biol. Open.* 1:711–722. https://doi.org/10.1242/bio.20121867

Bravo-Cordero, J.J., R. Marrero-Diaz, D. Megías, L. Genís, A. García-Grande, M.A. García, A.G. Arroyo, and M.C. Montoya. 2007. MT1-MMP proinvasive activity is regulated by a novel Rab8-dependent exocytic pathway. *EMBO J.* 26:1499–1510. https://doi.org/10.1038/sj.emboj.7601606

Bravo-Cordero, J.J., M. Oser, X. Chen, R. Eddy, L. Hodgson, and J. Condeelis. 2011. A novel spatiotemporal RhoC activation pathway locally regulates cofilin activity at invadopodia. *Curr. Biol.* 21:635–644. https://doi.org/10.1016/j.cub.2011.03.039

Bravo-Cordero, J.J., V.P. Sharma, M. Roh-Johnson, X. Chen, R. Eddy, J. Condeelis, and L. Hodgson. 2013. Spatial regulation of RhoC activity defines protrusion formation in migrating cells. *J. Cell Sci.* 126:3356–3369. https://doi.org/10.1242/jcs.123547

Buccione, R., G. Caldieri, and I. Ayala. 2009. Invadopodia: specialized tumor cell structures for the focal degradation of the extracellular matrix. *Cancer Metastasis Rev.* 28:137–149. https://doi.org/10.1007/s10555-008-9176-1

Castro-Castro, A., V. Marchesin, P. Monteiro, C. Lodillinsky, C. Rossé, and P. Chavrier. 2016. Cellular and Molecular Mechanisms of MT1-MMP-Dependent Cancer Cell Invasion. *Annu. Rev. Cell Dev. Biol.* 32:555–576. https://doi.org/10.1146/annurev-cellbio-111315-125227

Chan, A.Y., S.J. Coniglio, Y.Y. Chuang, D. Michaelson, U.G. Knaus, M.R. Philips, and M. Symons. 2005. Roles of the Rac1 and Rac3 GTPases in human tumor cell invasion. *Oncogene.* 24:7821–7829. https://doi.org/10.1038/sj.onc.1208909

Chen, W.T. 1989. Proteolytic activity of specialized surface protrusions formed at rosette contact sites of transformed cells. *J. Exp. Zool.* 251:167–185. https://doi.org/10.1002/jez.1402510206

Chen, W.T., and J.Y. Wang. 1999. Specialized surface protrusions of invasive cells, invadopodia and lamellipodia, have differential MT1-MMP, MMP-2, and TIMP-2 localization. *Ann. N. Y. Acad. Sci.* 878(1 INHIBITION OF):361–371. https://doi.org/10.1111/j.1749-6632.1999.tb07695.x

Clark, E.S., A.S. Whigham, W.G. Yarbrough, and A.M. Weaver. 2007. Cortactin is an essential regulator of matrix metalloproteinase secretion and extracellular matrix degradation in invadopodia. *Cancer Res.* 67:4227–4235. https://doi.org/10.1158/0008-5472.CAN-06-3928

Condeelis, J., R.H. Singer, and J.E. Segall. 2005. The great escape: when cancer cells hijack the genes for chemotaxis and motility. *Annu. Rev. Cell Dev. Biol.* 21:695–718. https://doi.org/10.1146/annurev.cellbio.21.122303.120306

Corbetta, S., S. Gualdoni, G. Ciceri, M. Monari, E. Zuccaro, V.L. Tybulewicz, and I. de Curtis. 2009. Essential role of Rac1 and Rac3 GTPases in neuronal development. *FASEB J.* 23:1347–1357. https://doi.org/10.1096/fj.08-121574

Courtneidge, S.A. 2012. Cell migration and invasion in human disease: the Tks adaptor proteins. *Biochem. Soc. Trans.* 40:129–132. https://doi.org/10.1042/BST20110685

Desai, B., T. Ma, and M.A. Chellaiah. 2008. Invadopodia and matrix degradation, a new property of prostate cancer cells during migration and invasion. *J. Biol. Chem.* 283:13856–13866. https://doi.org/10.1074/jbc.M709401200

Destaing, O., M.R. Block, E. Planus, and C. Albiges-Rizo. 2011. Invadosome regulation by adhesion signaling. *Curr. Opin. Cell Biol.* 23:597–606. https://doi.org/10.1016/j.ceb.2011.04.002

Eddy, R.J., M.D. Weidmann, V.P. Sharma, and J.S. Condeelis. 2017. Tumor Cell Invadopodia: Invasive Protrusions that Orchestrate Metastasis. *Trends Cell Biol.* 27:595–607. https://doi.org/10.1016/j.tcb.2017.03.003

Efron, B., and R. Tibshirani. 1993. An Introduction to the bootstrap. Chapman & Hall, New York. 436 pp. https://doi.org/10.1007/978-1-4899-4541-9

Engers, R., S. Ziegler, M. Mueller, A. Walter, R. Willers, and H.E. Gabbert. 2007. Prognostic relevance of increased Rac GTPase expression in prostate carcinomas. *Endocr. Relat. Cancer.* 14:245–256. https://doi.org/10.1677/ERC-06-0036

Fidler, I.J. 2003. The pathogenesis of cancer metastasis: the 'seed and soil' hypothesis revisited. *Nat. Rev. Cancer.* 3:453–458. https://doi.org/10.1038/nrc1098

Freeman, T.C. Jr., J.L. Black, H.G. Bray, O. Dagliyan, Y.I. Wu, A. Tripathy, N.V. Dokholyan, T.M. Leisner, and L.V. Parise. 2013. Identification of novel integrin binding partners for calcium and integrin binding protein 1 (CIB1): structural and thermodynamic basis of CIB1 promiscuity. *Biochemistry.* 52:7082–7090. https://doi.org/10.1021/bi400678y

Frittoli, E., A. Palamidessi, P. Marighetti, S. Confalonieri, F. Bianchi, C. Malinverno, G. Mazzarol, G. Viale, I. Martin-Padura, M. Garré, et al. 2014. A RAB5/RAB4 recycling circuitry induces a proteolytic invasive program and promotes tumor dissemination. *J. Cell Biol.* 206:307–328. https://doi.org/10.1083/jcb.201403127

Gest, C., U. Joimel, L. Huang, L.L. Pritchard, A. Petit, C. Dulong, C. Buquet, C.Q. Hu, P. Mirshahi, M. Laurent, et al. 2013. Rac3 induces a molecular pathway triggering breast cancer cell aggressiveness: differences in MDA-MB-231 and MCF-7 breast cancer cell lines. *BMC Cancer.* 13:63. https://doi.org/10.1186/1471-2407-13-63

Gimona, M., R. Buccione, S.A. Courtneidge, and S. Linder. 2008. Assembly and biological role of podosomes and invadopodia. *Curr. Opin. Cell Biol.* 20:235–241. https://doi.org/10.1016/j.ceb.2008.01.005

Gligorijevic, B., J. Wyckoff, H. Yamaguchi, Y. Wang, E.T. Roussos, and J. Condeelis. 2012. N-WASP-mediated invadopodium formation is involved in intravasation and lung metastasis of mammary tumors. *J. Cell Sci.* 125:724–734. https://doi.org/10.1242/jcs.092726

Haataja, L., J. Groffen, and N. Heisterkamp. 1997. Characterization of RAC3, a novel member of the Rho family. *J. Biol. Chem.* 272:20384–20388. https://doi.org/10.1074/jbc.272.33.20384

Haataja, L., V. Kaartinen, J. Groffen, and N. Heisterkamp. 2002. The small GTPase Rac3 interacts with the integrin-binding protein CIB and promotes integrin alpha(IIb)beta(3)-mediated adhesion and spreading. *J. Biol. Chem.* 277:8321–8328. https://doi.org/10.1074/jbc.M105363200

Hagedorn, E.J., L.C. Kelley, K.M. Naegeli, Z. Wang, Q. Chi, and D.R. Sherwood. 2014. ADF/cofilin promotes invadopodial membrane recycling during cell invasion in vivo. *J. Cell Biol.* 204:1209–1218. https://doi.org/10.1083/jcb.201312098

Hajdo-Milasinovic, A., S.I. Ellenbroek, S. van Es, B. van der Vaart, and J.G. Collard. 2007. Rac1 and Rac3 have opposing functions in cell adhesion and differentiation of neuronal cells. *J. Cell Sci.* 120:555–566. https://doi.org/10.1242/jcs.03364

Hajdo-Milasinovic, A., R.A. van der Kammen, Z. Moneva, and J.G. Collard. 2009. Rac3 inhibits adhesion and differentiation of neuronal cells by modifying GIT1 downstream signaling. *J. Cell Sci.* 122:2127–2136. https://doi.org/10.1242/jcs.039958

Hall, A. 2005. Rho GTPases and the control of cell behaviour. *Biochem. Soc. Trans.* 33:891–895. https://doi.org/10.1042/BST0330891

Hashimoto, S., Y. Onodera, A. Hashimoto, M. Tanaka, M. Hamaguchi, A. Yamada, and H. Sabe. 2004. Requirement for Arf6 in breast cancer invasive activities. *Proc. Natl. Acad. Sci. USA.* 101:6647–6652. https://doi.org/10.1073/pnas.0401753101

Hastie, E.L., and D.R. Sherwood. 2016. A new front in cell invasion: The invadopodial membrane. *Eur. J. Cell Biol.* 95:441–448. https://doi.org/10.1016/j.ejcb.2016.06.006

Hodgson, L., O. Pertz, and K.M. Hahn. 2008. Design and optimization of genetically encoded fluorescent biosensors: GTPase biosensors. *Methods Cell Biol.* 85:63–81. https://doi.org/10.1016/S0091-679X(08)85004-2

Hoshino, D., K.M. Branch, and A.M. Weaver. 2013. Signaling inputs to invadopodia and podosomes. *J. Cell Sci.* 126:2979–2989. https://doi.org/10.1242/jcs.079475

Hwang, S.L., J.H. Chang, T.S. Cheng, W.D. Sy, A.S. Lieu, C.L. Lin, K.S. Lee, S.L. Howng, and Y.R. Hong. 2005. Expression of Rac3 in human brain tumors. *J. Clin. Neurosci.* 12:571–574.

Ioannou, M.S., E.S. Bell, M. Girard, M. Chaineau, J.N. Hamlin, M. Daubaras, A. Monast, M. Park, L. Hodgson, and P.S. McPherson. 2015. DENND2B activates Rab13 at the leading edge of migrating cells and promotes metastatic behavior. *J. Cell Biol.* 208:629–648. https://doi.org/10.1083/jcb.201407068

Jimenez, L., V.P. Sharma, J. Condeelis, T. Harris, T.J. Ow, M.B. Prystowsky, G. Childs, and J.E. Segall. 2015. MicroRNA Suppresses Extracellular Matrix Degradation and Ivadopodial Activity in Head and Neck Squamous Cell Carcinoma. *Arch. Pathol. Lab. Med.* 139:1349–1361.

Jones, M.C., K. Machida, B.J. Mayer, and C.E. Turner. 2013. Paxillin kinase linker (PKL) regulates Vav2 signaling during cell spreading and migration. *Mol. Biol. Cell.* 24:1882–1894. https://doi.org/10.1091/mbc.E12-09-0654

Linder, S., C. Wiesner, and M. Himmel. 2011. Degrading devices: invadosomes in proteolytic cell invasion. *Annu. Rev. Cell Dev. Biol.* 27:185–211. https://doi.org/10.1146/annurev-cellbio-092910-154216

Lohmer, L.L., L.C. Kelley, E.J. Hagedorn, and D.R. Sherwood. 2014. Invadopodia and basement membrane invasion in vivo. *Cell Adhes. Migr.* 8:246–255. https://doi.org/10.4161/cam.28406

Machacek, M., L. Hodgson, C. Welch, H. Elliott, O. Pertz, P. Nalbant, A. Abell, G.L. Johnson, K.M. Hahn, and G. Danuser. 2009. Coordination of Rho GTPase activities during cell protrusion. *Nature.* 461:99–103. https://doi.org/10.1038/nature08242

Mader, C.C., M. Oser, M.A. Magalhaes, J.J. Bravo-Cordero, J. Condeelis, A.J. Koleske, and H. Gil-Henn. 2011. An EGFR-Src-Arg-cortactin pathway mediates functional maturation of invadopodia and breast cancer cell invasion. *Cancer Res.* 71:1730–1741. https://doi.org/10.1158/0008-5472.CAN-10-1432

Magalhaes, M.A., D.R. Larson, C.C. Mader, J.J. Bravo-Cordero, H. Gil-Henn, M. Oser, X. Chen, A.J. Koleske, and J. Condeelis. 2011. Cortactin

phosphorylation regulates cell invasion through a pH-dependent pathway. *J. Cell Biol.* 195:903–920. https://doi.org/10.1083/jcb.201103045

Marchesin, V., A. Castro-Castro, C. Lodillinsky, A. Castagnino, J. Cyrta, H. Bonsang-Kitzis, L. Fuhrmann, M. Irondelle, E. Infante, G. Montagnac, et al. 2015. ARF6-JIP3/4 regulate endosomal tubules for MT1-MMP exocytosis in cancer invasion. *J. Cell Biol.* 211:339–358. https://doi.org/10.1083/jcb.201506002

Mayhew, M.W., D.J. Webb, M. Kovalenko, L. Whitmore, J.W. Fox, and A.F. Horwitz. 2006. Identification of protein networks associated with the PAK1-betaPIX-GIT1-paxillin signaling complex by mass spectrometry. *J. Proteome Res.* 5:2417–2423. https://doi.org/10.1021/pr060140t

Miskolci, V., B. Wu, Y. Moshfegh, D. Cox, and L. Hodgson. 2016. Optical Tools To Study the Isoform-Specific Roles of Small GTPases in Immune Cells. *J. Immunol.* 196:3479–3493. https://doi.org/10.4049/jimmunol.1501655

Monteiro, P., C. Rossé, A. Castro-Castro, M. Irondelle, E. Lagoutte, P. Paul-Gilloteaux, C. Desnos, E. Formstecher, F. Darchen, D. Perrais, et al. 2013. Endosomal WASH and exocyst complexes control exocytosis of MT1-MMP at invadopodia. *J. Cell Biol.* 203:1063–1079. https://doi.org/10.1083/jcb.201306162

Moores, S.L., L.M. Selfors, J. Fredericks, T. Breit, K. Fujikawa, F.W. Alt, J.S. Brugge, and W. Swat. 2000. Vav family proteins couple to diverse cell surface receptors. *Mol. Cell. Biol.* 20:6364–6373. https://doi.org/10.1128/MCB.20.17.6364-6373.2000

Moshfegh, Y., J.J. Bravo-Cordero, V. Miskolci, J. Condeelis, and L. Hodgson. 2014. A Trio-Rac1-Pak1 signalling axis drives invadopodia disassembly. *Nat. Cell Biol.* 16:574–586. https://doi.org/10.1038/ncb2972

Neri, A., and G.L. Nicolson. 1981. Phenotypic drift of metastatic and cell-surface properties of mammary adenocarcinoma cell clones during growth in vitro. *Int. J. Cancer.* 28:731–738. https://doi.org/10.1002/ijc.2910280612

Nicholas, N.S., A. Pipili, M.S. Lesjak, S.M. Ameer-Beg, J.L. Geh, C. Healy, A.D. MacKenzie Ross, M. Parsons, F.O. Nestle, K.E. Lacy, and C.M. Wells. 2016. PAK4 suppresses PDZ-RhoGEF activity to drive invadopodia maturation in melanoma cells. *Oncotarget.* 7:70881–70897.

Oser, M., H. Yamaguchi, C.C. Mader, J.J. Bravo-Cordero, M. Arias, X. Chen, V. Desmarais, J. van Rheenen, A.J. Koleske, and J. Condeelis. 2009. Cortactin regulates cofilin and N-WASp activities to control the stages of invadopodium assembly and maturation. *J. Cell Biol.* 186:571–587. https://doi.org/10.1083/jcb.200812176

Parekh, A., N.S. Ruppender, K.M. Branch, M.K. Sewell-Loftin, J. Lin, P.D. Boyer, J.E. Candiello, W.D. Merryman, S.A. Guelcher, and A.M. Weaver. 2011. Sensing and modulation of invadopodia across a wide range of rigidities. *Biophys. J.* 100:573–582. https://doi.org/10.1016/j.bpj.2010.12.3733

Paz, H., N. Pathak, and J. Yang. 2014. Invading one step at a time: the role of invadopodia in tumor metastasis. *Oncogene.* 33:4193–4202. https://doi.org/10.1038/onc.2013.393

Pertz, O., L. Hodgson, R.L. Klemke, and K.M. Hahn. 2006. Spatiotemporal dynamics of RhoA activity in migrating cells. *Nature.* 440:1069–1072. https://doi.org/10.1038/nature04665

Reinhard, N.R., S.F. van Helden, E.C. Anthony, T. Yin, Y.I. Wu, J. Goedhart, T.W. Gadella, and P.L. Hordijk. 2016. Spatiotemporal analysis of RhoA/B/C activation in primary human endothelial cells. *Sci. Rep.* 6:25502. https://doi.org/10.1038/srep25502

Roh-Johnson, M., J.J. Bravo-Cordero, A. Patsialou, V.P. Sharma, P. Guo, H. Liu, L. Hodgson, and J. Condeelis. 2014. Macrophage contact induces RhoA GTPase signaling to trigger tumor cell intravasation. *Oncogene.* 33:4203–4212. https://doi.org/10.1038/onc.2013.377

Rosenberg, B.J., H. Gil-Henn, C.C. Mader, T. Halo, T. Yin, J. Condeelis, K. Machida, Y.I. Wu, and A.J. Koleske. 2017. Phosphorylated cortactin recruits Vav2 guanine nucleotide exchange factor to activate Rac3 and promote invadopodial function in invasive breast cancer cells. *Mol. Biol. Cell.* 28:1347–1360. https://doi.org/10.1091/mbc.E16-12-0885

Rosenberger, G., and K. Kutsche. 2006. AlphaPIX and betaPIX and their role in focal adhesion formation. *Eur. J. Cell Biol.* 85:265–274. https://doi.org/10.1016/j.ejcb.2005.10.007

Sakurai-Yageta, M., C. Recchi, G. Le Dez, J.B. Sibarita, L. Daviet, J. Camonis, C. D'Souza-Schorey, and P. Chavrier. 2008. The interaction of IQGAP1 with the exocyst complex is required for tumor cell invasion downstream of Cdc42 and RhoA. *J. Cell Biol.* 181:985–998. https://doi.org/10.1083/jcb.200709076

Sanjana, N.E., O. Shalem, and F. Zhang. 2014. Improved vectors and genome-wide libraries for CRISPR screening. *Nat. Methods.* 11:783–784. https://doi.org/10.1038/nmeth.3047

Schmitz, A.A., E.E. Govek, B. Böttner, and L. Van Aelst. 2000. Rho GTPases: signaling, migration, and invasion. *Exp. Cell Res.* 261:1–12. https://doi.org/10.1006/excr.2000.5049

Shalem, O., N.E. Sanjana, E. Hartenian, X. Shi, D.A. Scott, T. Mikkelson, D. Heckl, B.L. Ebert, D.E. Root, J.G. Doench, and F. Zhang. 2014. Genome-scale CRISPR-Cas9 knockout screening in human cells. *Science.* 343:84–87. https://doi.org/10.1126/science.1247005

Shcherbakova, D.M., M. Baloban, A.V. Emelyanov, M. Brenowitz, P. Guo, and V.V. Verkhusha. 2016. Bright monomeric near-infrared fluorescent proteins as tags and biosensors for multiscale imaging. *Nat. Commun.* 7:12405. https://doi.org/10.1038/ncomms12405

Shin, E.Y., K.S. Shin, C.S. Lee, K.N. Woo, S.H. Quan, N.K. Soung, Y.G. Kim, C.I. Cha, S.R. Kim, D. Park, et al. 2002. Phosphorylation of p85 beta PIX, a Rac/Cdc42-specific guanine nucleotide exchange factor, via the Ras/ERK/PAK2 pathway is required for basic fibroblast growth factor-induced neurite outgrowth. *J. Biol. Chem.* 277:44417–44430. https://doi.org/10.1074/jbc.M203754200

Spiering, D., and L. Hodgson. 2012. Multiplex imaging of Rho family GTPase activities in living cells. *Methods Mol. Biol.* 827:215–234. https://doi.org/10.1007/978-1-61779-442-1_15

Spiering, D., J.J. Bravo-Cordero, Y. Moshfegh, V. Miskolci, and L. Hodgson. 2013. Quantitative ratiometric imaging of FRET-biosensors in living cells. *Methods Cell Biol.* 114:593–609. https://doi.org/10.1016/B978-0-12-407761-4.00025-7

Theodosiou, M., M. Widmaier, R.T. Böttcher, E. Rognoni, M. Veelders, M. Bharadwaj, A. Lambacher, K. Austen, D.J. Müller, R. Zent, and R. Fässler. 2016. Kindlin-2 cooperates with talin to activate integrins and induces cell spreading by directly binding paxillin. *eLife.* 5:e10130. https://doi.org/10.7554/eLife.10130

Turner, C.E. 2000. Paxillin interactions. *J. Cell Sci.* 113:4139–4140.

Vaghi, V., R. Pennucci, F. Talpo, S. Corbetta, V. Montinaro, C. Barone, L. Croci, P. Spaiardi, G.G. Consalez, G. Biella, and I. de Curtis. 2012. Rac1 and Rac3 GTPases Control Synergistically the Development of Cortical and Hippocampal GABAergic Interneurons. Cerebral cortex. *Cereb. Cortex.* 24:1247–1258. https://doi.org/10.1093/cercor/bhs402

Vallar, L., C. Melchior, S. Plançon, H. Drobecq, G. Lippens, V. Regnault, and N. Kieffer. 1999. Divalent cations differentially regulate integrin alphaIIb cytoplasmic tail binding to beta3 and to calcium- and integrin-binding protein. *J. Biol. Chem.* 274:17257–17266. https://doi.org/10.1074/jbc.274.24.17257

Vitale, N., W.A. Patton, J. Moss, M. Vaughan, R.J. Lefkowitz, and R.T. Premont. 2000. GIT proteins, A novel family of phosphatidylinositol 3,4,5-trisphosphate-stimulated GTPase-activating proteins for ARF6. *J. Biol. Chem.* 275:13901–13906. https://doi.org/10.1074/jbc.275.18.13901

Wang, W., J.B. Wyckoff, Y. Wang, E.P. Bottinger, J.E. Segall, and J.S. Condeelis. 2003. Gene expression analysis on small numbers of invasive cells collected by chemotaxis from primary mammary tumors of the mouse. *BMC Biotechnol.* 3:13. https://doi.org/10.1186/1472-6750-3-13

White, M.A., C. Nicolette, A. Minden, A. Polverino, L. Van Aelst, M. Karin, and M.H. Wigler. 1995. Multiple Ras functions can contribute to mammalian cell transformation. *Cell.* 80:533–541. https://doi.org/10.1016/0092-8674(95)90507-3

Whitlow, M., B.A. Bell, S.-L. Feng, D. Filpula, K.D. Hardman, S.L. Hubert, M.L. Rollence, J.F. Wood, M.E. Schott, D.E. Milenic, et al. 1993. An improved linker for single-chain Fv with reduced aggregation and enhanced proteolytic stability. *Protein Eng.* 6:989–995. https://doi.org/10.1093/protein/6.8.989

Wu, B., V. Miskolci, H. Sato, E. Tutucci, C.A. Kenworthy, S.K. Donnelly, Y.J. Yoon, D. Cox, R.H. Singer, and L. Hodgson. 2015. Synonymous modification results in high-fidelity gene expression of repetitive protein and nucleotide sequences. *Genes Dev.* 29:876–886. https://doi.org/10.1101/gad.259358.115

Yamaguchi, H., J. Wyckoff, and J. Condeelis. 2005. Cell migration in tumors. *Curr. Opin. Cell Biol.* 17:559–564. https://doi.org/10.1016/j.ceb.2005.08.002

Yu, X., T. Zech, L. McDonald, E.G. Gonzalez, A. Li, I. Macpherson, J.P. Schwarz, H. Spence, K. Futó, P. Timpson, et al. 2012. N-WASP coordinates the delivery and F-actin-mediated capture of MT1-MMP at invasive pseudopods. *J. Cell Biol.* 199:527–544. https://doi.org/10.1083/jcb.201203025

Zhang, Y., L.A. Rivera Rosado, S.Y. Moon, and B. Zhang. 2009. Silencing of D4-GDI inhibits growth and invasive behavior in MDA-MB-231 cells by activation of Rac-dependent p38 and JNK signaling. *J. Biol. Chem.* 284:12956–12965. https://doi.org/10.1074/jbc.M807845200

Zhou, Z.N., V.P. Sharma, B.T. Beaty, M. Roh-Johnson, E.A. Peterson, N. Van Rooijen, P.A. Kenny, H.S. Wiley, J.S. Condeelis, and J.E. Segall. 2014. Autocrine HBEGF expression promotes breast cancer intravasation, metastasis and macrophage-independent invasion in vivo. *Oncogene.* 33:3784–3793. https://doi.org/10.1038/onc.2013.363

Zhu, W.L., M.S. Hossain, D.Y. Guo, S. Liu, H. Tong, A. Khakpoor, P.J. Casey, and M. Wang. 2011. A role for Rac3 GTPase in the regulation of autophagy. *J. Biol. Chem.* 286:35291–35298. https://doi.org/10.1074/jbc.M111.280990